

CO emission and CO hotspots in diffuse molecular gas

HARVEY S. LISZT¹

¹*National Radio Astronomy Observatory
520 Edgemont Road, Charlottesville, VA, 22903-2475*

(Dated: generated June 1, 2020)

ABSTRACT

We observed $\lambda 3\text{mm}$ ^{12}CO , ^{13}CO , C^{18}O , HCO^+ , HCN and CS emission from diffuse molecular gas along sightlines with $E_{\text{B-V}} \approx 0.1 - 1$ mag. Directions were mostly chosen for their proximity to sightlines toward background mm-wave continuum sources studied in HCO^+ absorption, at positions where maps of ^{12}CO at $1'$ resolution showed surprisingly bright integrated CO J=1-0 emission $W_{\text{CO}} = 5\text{-}12$ K-km s⁻¹ but we also observed in L121 near ζ Oph. Coherence emerges when data are considered over a broad range of ^{12}CO and ^{13}CO brightness. W_{CO}/W_{13} and $N(^{12}\text{CO})/N(^{13}\text{CO})$ are 20-40 for $W_{\text{CO}} \lesssim 5$ K-km s⁻¹ and $N(\text{CO}) \lesssim 5 \times 10^{15}$ cm⁻², increasing with much scatter for larger W_{CO} or $N(\text{CO})$. $N(^{13}\text{CO})/N(\text{C}^{18}\text{O}) > 20\text{-}40$ (3σ) vs. an intrinsic ratio $^{13}\text{C}/^{18}\text{O} = 8.4$, from a combination of selective photodissociation and enhancement of ^{13}CO . The observations are understandable if ^{12}CO forms from the thermal recombination of HCO^+ with electrons, after which the observed ^{13}CO forms via endothermic carbon isotope exchange with $^{13}\text{C}^+$. $W_{\text{CS}}/W_{\text{CO}}$ increases abruptly for $W_{\text{CO}} \gtrsim 10$ K-km s⁻¹ and $W_{\text{CS}}/W_{\text{HCO}^+}$ is bimodal, showing two branches having $N(\text{CS})/N(\text{HCO}^+) \approx 5$ and 1.25. Because CO formation and HCO^+ excitation both involve collisions between HCO^+ and ambient electrons, comparison of the CO and HCO^+ emission shows that the CO hotspots are small regions of enhanced $N(\text{CO})$ occupying only a small fraction of the column density of the medium in which they are embedded. HCO^+/CO and HCN/CO brightness ratios are 1-2% with obvious implications for determinations of the true dense gas fraction.

Keywords: astrochemistry . ISM: molecules . ISM: clouds. Galaxy

1. INTRODUCTION

The sky viewed in CO J=1-0 $\lambda 2.6\text{mm}$ emission (Dame et al. 2001) is usually understood as the map of molecular gas, showing the locations of the Galactic molecular clouds. CO emission and molecular gas are synonymous, even to the extent that a linear scaling of the integrated CO bright-

ness W_{CO} (with units of K-km s⁻¹), with appropriate caveats, gives $N(\text{H}_2)$ via the CO-H₂ conversion factor (Bolatto et al. 2013).

Interpretation of the CO sky map is complicated by the presence of emission arising in partially molecular gas having a significant admixture of atomic hydrogen, small CO column densities and small CO abundances. CO lines from this so-called diffuse or diffuse molecular gas can be quite bright at $E_{\text{B-V}} \lesssim 0.3$ mag, $W_{\text{CO}} \approx 5\text{-}$

10 K-km s⁻¹, mimicking emission from traditional dark clouds (Liszt et al. 2009; Liszt & Pety 2012). For example, the mean reddening toward the catalog positions of the MBM high-latitude molecular cloud complexes (Magnani et al. 1985) is only 0.28±0.24 mag. Free gas-phase carbon is predominantly in the form of C⁺, not CO, under such conditions.

Thus it is not solely a matter of observing how much of the sky is occupied by CO emission, but also of assessing where the emission arises and what it means beyond a simple scaling to N(H₂). The importance of accounting for H₂ in partially-molecular gas at low-moderate optical extinction is only reinforced by the recognition that the extinction is actually quite modest over large portions of large cloud complexes like Taurus (Goldsmith et al. 2008) or Chamaeleon (Planck Collaboration et al. 2015) and that conversion of CO brightness to N(H₂) is fraught with difficulty (Goldsmith et al. 2008) when isotopic fractionation and non-LTE excitation are the rule.

Moreover CO emission fails to represent substantial amounts of H₂ in partially-molecular gas at the HI→H₂ transition (Grenier et al. 2005; Wolfire et al. 2010). When significant amounts of gas are missed in a combined census of CO and HI emission – the so-called dark neutral medium (DNM) (Planck Collaboration et al. 2015) – molecular gas is detectable in mm-wave absorption from HCO⁺, C₂H and other small molecules (Liszt et al. 2018) and the absence of detectable CO emission can be attributed to small CO column densities that are nonetheless detectable in mm-wave absorption thanks to the power of modern mm-wave telescopes (Liszt et al. 2019). In Chamaeleon, the DNM missing in CO and/or HI emission in the outskirts of the complex turns out to be primarily molecular, even while the outlying medium is mostly but not overwhelmingly atomic.

In this work we present a somewhat eclectic (but ultimately coherent) assortment of new λ 3mm emission-line observations of carbon monox-

ide and more strongly-polar molecules HCO⁺ and CS toward and around previously-known (Liszt & Pety 2012) and newly-identified positions having relatively intense CO emission at modest reddening, so-called CO hotspots where $W_{\text{CO}} = 5\text{-}10$ K-km s⁻¹. Section 2 describes the circumstances of the new and existing observations that are discussed. Section 3 is a source-by-source presentation of the data. Results for the carbon monoxide isotopologues are gathered and modelled in Section 4. Results for more strongly-polar species, chiefly the HCO⁺ J=1-0 and CS J=2-1 lines, are discussed in Section 5 where the CO hotspots around mm-wave continuum background sources having $W_{\text{CO}} = 5\text{-}10$ K-km s⁻¹ are interpreted as regions of enhanced H₂ and CO formation that are expected from models of turbulent gas at the HI→H₂ transition. Section 6 is a summary where we also discuss the relevance of the present results to observations of the Milky Way and other galaxies.

2. OBSERVATIONS AND MODELLING

2.1. *New data*

The new data shown here were taken at the ARO Kitt Peak 12m telescope during several observing runs in December or April during the period 2010-2012. Table 1 reprises some general target and sightline characteristics; coordinates, reddening, etc. Table 2 shows positions and profile integrals for the individual sightlines that furnish the observational material.

The ARO data are presented in terms of the customary brightness scale T_r^* extrapolated outside the atmosphere and nominally corrected for primary beam efficiency by an increase of a factor 1/0.85. As noted by Liszt et al. (2009) this scale is commensurate with the main beam brightness temperature scale of the Nanten telescope, as empirically verified by comparing observations with both instruments over the L121 cloud near ζ Oph. The LSR velocity scale uses the common kine-

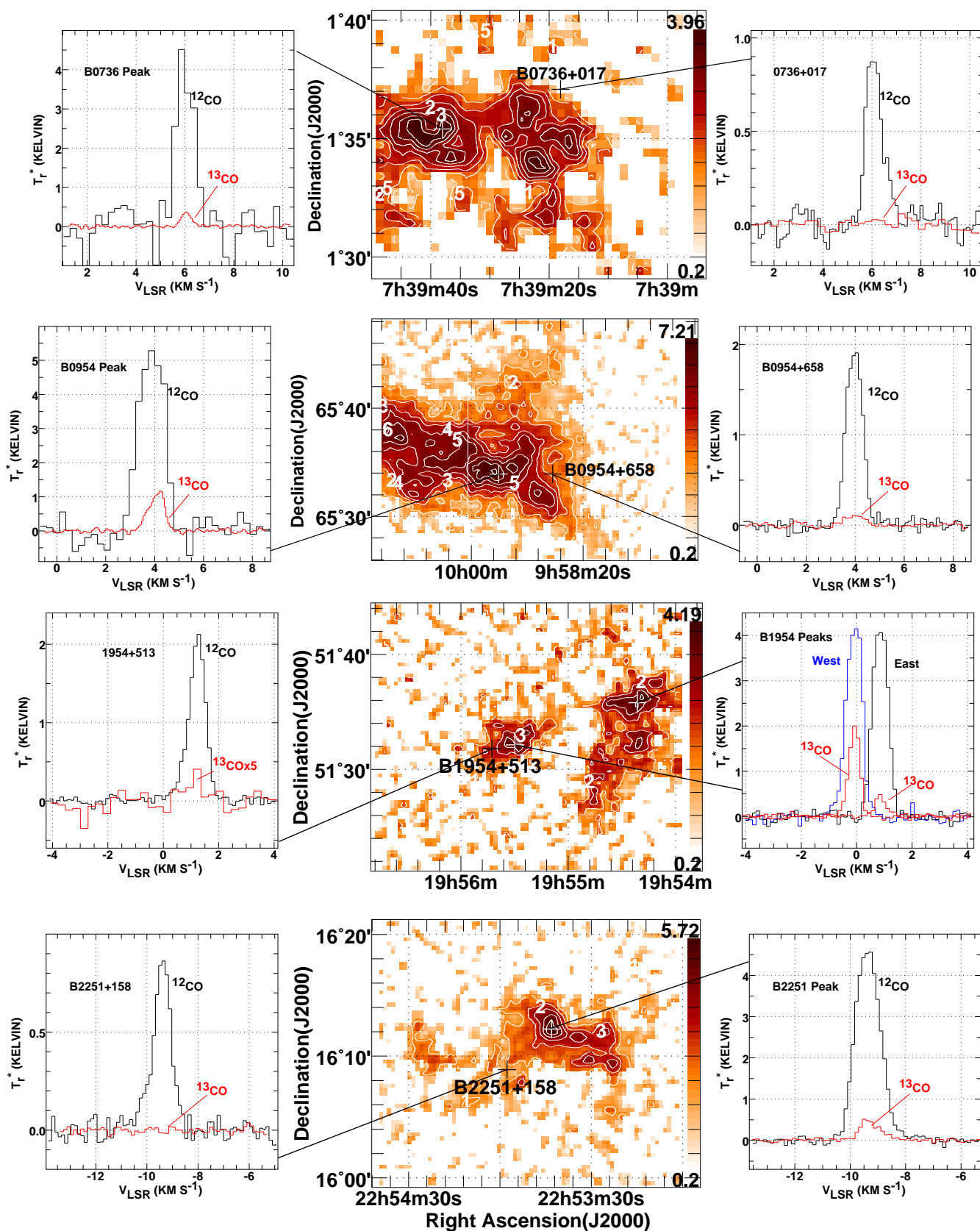


Figure 1. ^{12}CO and ^{13}CO emission around B0736, B0954, B1954 and B2251. In the center are maps of W_{CO} with the positions of the continuum source and one or more emission peaks indicated. Spectra toward the continuum and the peak positions are shown to either side. The contours are at levels 1, 2 .. 7 K km s^{-1} and the color scale on the maps at center varies between 0.2 K km s^{-1} and the peak value as shown at the upper end.

Table 1. Target, line of sight and map field properties

Target	ra J2000	dec J2000	l °	b °	Map size	E_{B-V} ¹ mag	$N(\text{H I})$ ² 10^{20} cm^{-2}	$N(\text{H}_2)$ ³ 10^{20} cm^{-2}	f_{H_2} ⁴	W_{CO} K km
B0528+134	05:30:46.41	13:31:55.1	191.37	-11.01	30'	0.89	23.3	7.9	0.40	2.
B0736+017	07:39:18.03	01:37:04.6	216.99	11.38	15'	0.13	8.0	3.3	0.45	0.
B0954+658	09:58:47.24	65:33:54.7	145.75	43.13	30'	0.12	4.7	4.8	0.67	1.
B1954+513	19:55:42.69	51.31:48.5	85.30	11.76	30'	0.15	11.4	5.0	0.47	1.
B2200+420	22:02:43.24	42:16:39.9	92.59	-10.44	30'	0.33	17.1	8.8	0.51	5.
B2251+158	22:53:57.71	16:08:53.4	86.11	-38.18	30'	0.10	7.2	1.2	0.25	0.
L121 peak	16:32:44.20	-12:09:48.1	4.53	22.9	90'	0.67	14.7			12

¹from [Schlegel et al. \(1998\)](#)² $N(\text{H I}) = 1.823 \times 10^{18} \text{ cm}^{-2} \int T_B(\text{HI}) dv$ with data from EBHIS or GASS III³ $N(\text{H}_2) = N(\text{HCO}^+)/3 \times 10^{-9}$ see Section 2.3⁴ $f_{\text{H}_2} = 2N(\text{H}_2)/(N(\text{H I}) + 2N(\text{H}_2))$, $\langle N(\text{H})/E_{B-V} \rangle = \Sigma N(\text{H})/\Sigma E_{B-V} = 7.63 \times 10^{21} \text{ cm}^{-2} \text{ mag}^{-1}$ ⁵ $X_{\text{CO}} = N(\text{H}_2)/W_{\text{CO}}$, units are $10^{20} \text{ cm}^{-2}/(\text{K-km s}^{-1})$. $\langle X_{\text{CO}} \rangle = \Sigma N(\text{H}_2)/\Sigma W_{\text{CO}} = 2.42 \times 10^{20} \text{ cm}^{-2} (\text{K-km s}^{-1})^{-1}$ ⁶ $X(\text{CO}) = (W_{\text{CO}} \times 10^{15} \text{ cm}^{-2})/N(\text{H}_2) \times 10^6$, $\langle X(\text{CO}) \rangle = \Sigma N(\text{CO})/\Sigma N(\text{H}_2) = 4.1 \times 10^{-6}$

matic definition that is universally employed at radio telescopes.

The new observations mostly consist of pointed, position-switched observations of species other than ^{12}CO toward peaks found in maps of ^{12}CO emission around the positions of compact extragalactic continuum sources used to study mm-wave absorption. The ^{12}CO maps used as finding charts were discussed in Liszt & Pety (2012) and the new observations should be understood in context with reference to their Figures showing the placement of the background targets maps of galactic reddening, noting their separation from regions of high extinction. However, we also observed at positions of ^{12}CO peaks toward portions of the L121 cloud that we identified in new ARO Kitt Peak 12m maps of ^{12}CO emission, and we made an on-the-fly map of ^{13}CO emission in the field around B0528-134. Nearby off-source positions for position-switching were already known from the extensive mapping we had done.

Observations toward all sources are discussed individually in the ensuing text but the overall goal of understanding the systematics of CO emission from diffuse molecular gas is really only approachable when the full ensemble of observations is examined.

Most of the new CO observations are of ^{13}CO , as the CO hotspots had previously only been observed in ^{12}CO . But we also searched for C^{18}O emission in some directions and we made extensive observations of the J=1-0 line of HCO^+ and more limited observations of CS J=2-1. The 1-0 lines of HCN, HNC, and C_2H were observed toward Peak 1 near BL Lac and are shown for the sake of completeness in Appendix B where their profile integrals are given. The $W_{\text{HCN}}/W_{\text{CO}}$ ratio at Peak 1 around BL Lac, 0.017 ± 0.001 , is discussed in Section 6.7.

All of the new pointed observations were observed at higher spectral resolution and smoothed to 49 kHz resolution or 0.13 km s^{-1} at 115.3 GHz. The ^{13}CO OTF mapping around B0528 had a resolution of 100 kHz or 0.27 km s^{-1} . In the compar-

isons below, some CO peaks were only observed in ^{12}CO during the earlier OTF mapping and these profiles have a resolution 100 kHz (0.26 km s^{-1} at 115.3 GHz).

2.2. Existing data

We show emission profiles from the CO mapping around continuum sources from which many of the peaks observed here were first identified (Liszt & Pety 2012) and we show pointed observations taken with higher spectral resolution toward the continuum sources themselves. We discuss CO line profile integrals toward a wider sample of continuum background sources observed by Liszt & Lucas (1998) (labelled PdBI or PdBI sightlines) and from the CO emission survey toward common UV absorption targets of Liszt (2008) and labelled ‘‘Survey 2008’’. Some CO emission data closer to ζ Oph were discussed by Liszt (1997) and these are labelled ζ Oph $\pm 30'$. We also discuss the ‘‘Mask 1’’ subset of CO emission brightnesses at low extinction in Taurus observed by Goldsmith et al. (2008).

In Section 6 we derive molecular hydrogen number and column densities by comparing emission and absorption profiles of the HCO^+ J=1-0 line, mostly taken from the work of Lucas & Liszt (1996) but augmented in a few cases with newer NOEMA absorption profiles of higher sensitivity and spectral resolution.

2.3. Modeling

In what follows we compare the observations with recently-published models of CO formation, excitation and fractionation (Liszt 2017). The models self-consistently calculate the equilibrium abundances of H_2 (Liszt 2015) and CO (Liszt 2007) and their isotopologues in uniformly illuminated, uniform density media having spherical geometry, in the presence of photodissociation, self- and mutual shielding, and exchange of carbon isotopes by the reaction of C^+ and CO. All aspects of the illumination (optical/UV, cosmic-ray, X-ray) are scaled by a parameter $G_0 = 1/3, 1/2$ and 1.

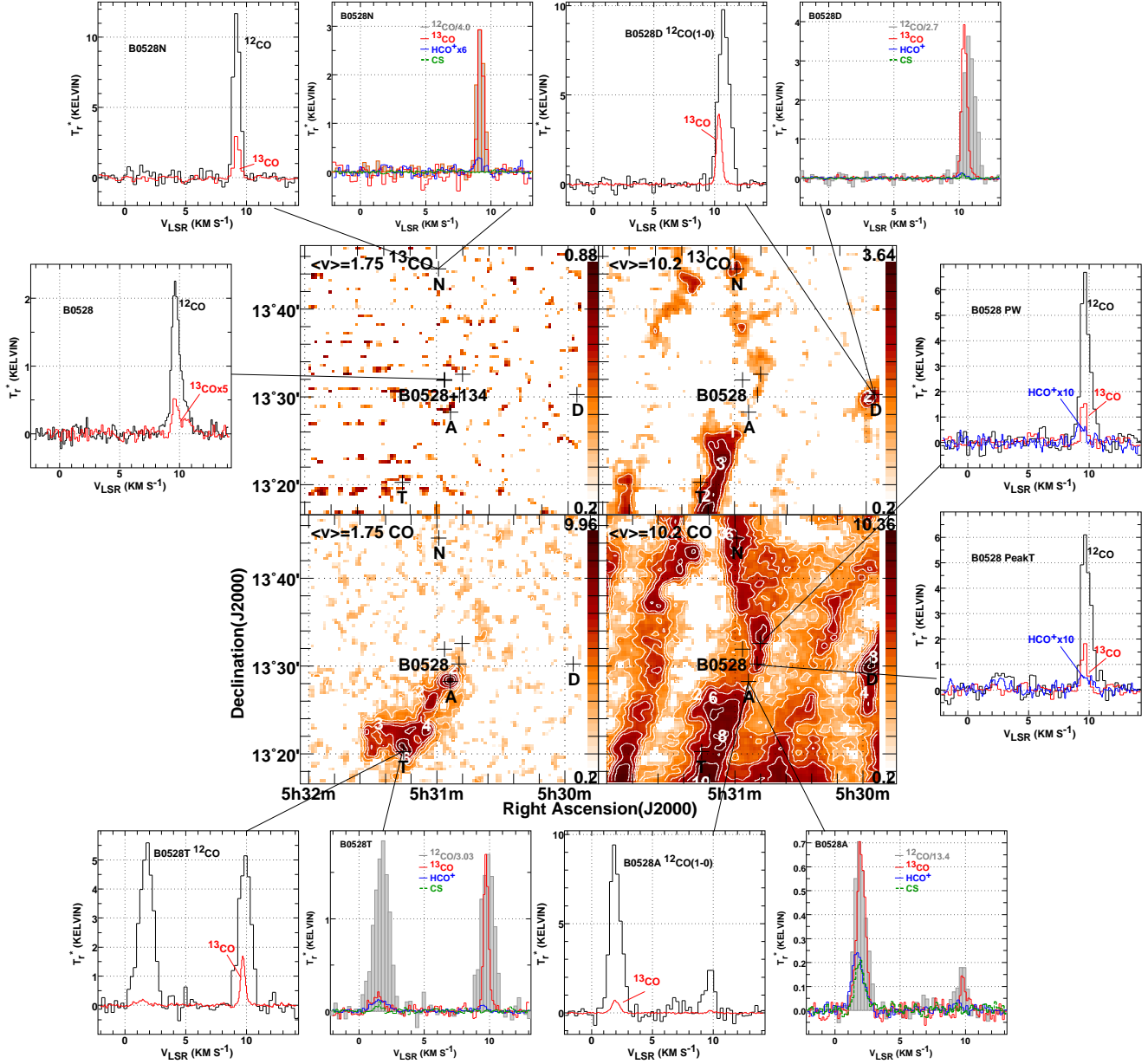


Figure 2. Molecular emission around B0528+134. At center are maps of ^{13}CO in the upper row and ^{12}CO at bottom, with the blue shifted gas at left and the red-shifted emission at right. The continuum and other selected locations are marked, with lines directed to the spectra at those positions. In some cases the same position is represented by two plots of spectra. Contours are at levels 1, 2, 3, 4, 6, 8 and 10 K km s^{-1} .

The CO chemistry is modeled under the simple assumption that the observed quantity of HCO^+ , $N(\text{HCO}^+)/N(\text{H}_2) = 3 \times 10^{-9}$ (Liszt et al. (2010) and Liszt & Gerin (2016)) recombines to form CO at the local kinetic temperature that is self-consistently computed in the models (Wolfire et al. 1995, 2003). It is actually possible to check the usefulness of this approach given the observed

HCO^+ emission as described in Section 5.1. This is because the formation of CO from the recombination of HCO^+ and the rotational excitation of HCO^+ both arise from the interaction of HCO^+ with free electrons.

The isotopologic abundance ratios $\text{HCO}^+/\text{H}^{13}\text{CO}^+/\text{HC}^{18}\text{O}^+$ in the model are taken as 1:1/62:1/520 so that the CO isotopologues are

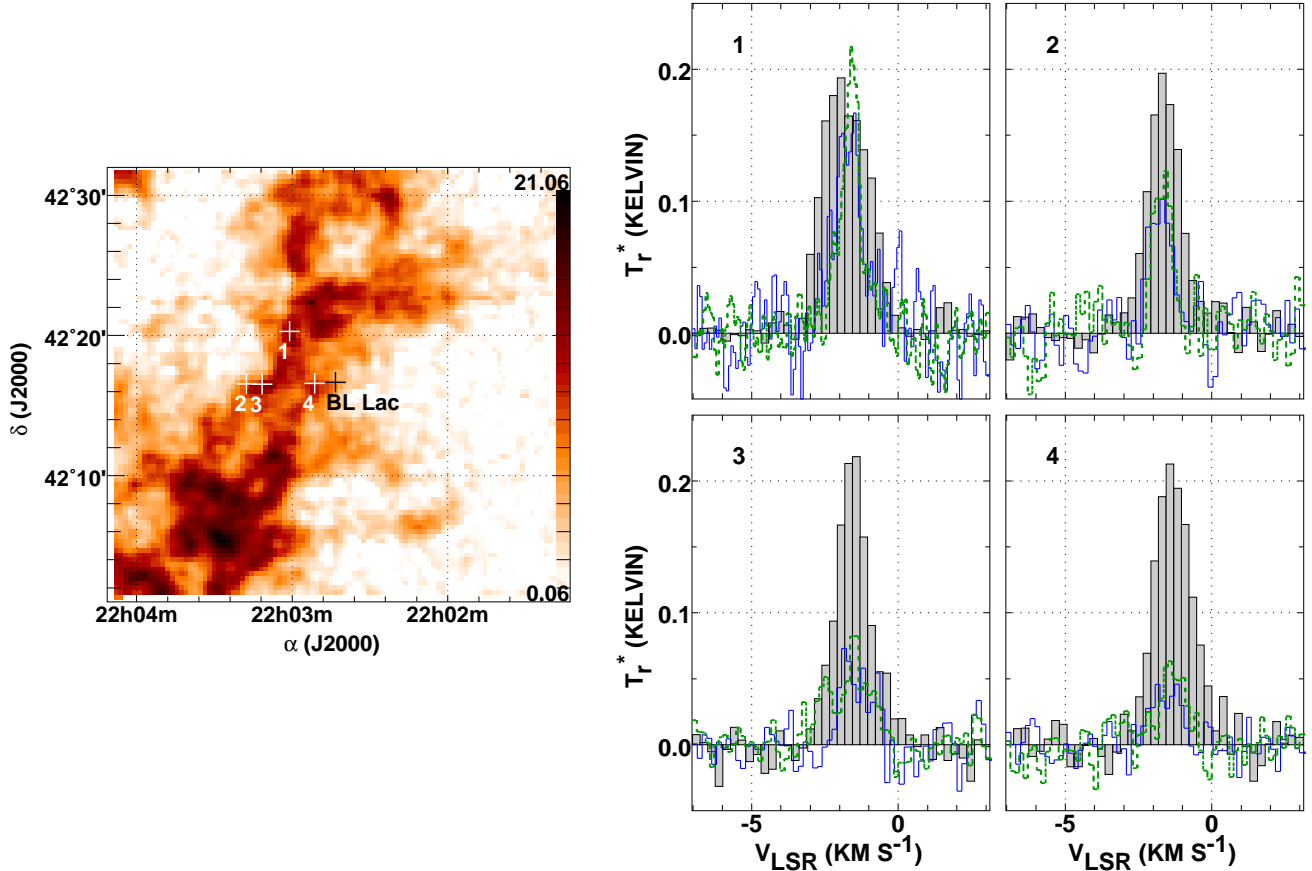


Figure 3. Molecular emission around BL Lac. At left is a map of W_{CO} , on which are marked the locations of BL Lac and four positions whose CO, HCO^+ , and CS spectra are shown at right. The CO profiles at right, shown gray and shaded, have been scaled downward by a factor 30. HCO^+ is shown as a blue histogram with full lines, CS is shown dashed and green.

formed in the same proportion as the inherent isotopic abundance ratios in the gas. It is not possible to fractionate HCO^+ through its chemical isotopic exchange reactions with CO (Roueff et al. 2015) in diffuse gas where the electron abundance is high, most of the carbon is in C^+ and the abundance of CO is small: This is the case because, unlike in dark clouds, HCO^+ recombines with electrons thousands of times more rapidly than it reacts with CO. The CO isotopologues are fractionated after formation through the processes of selective photodissociation and carbon isotope exchange at the local kinetic temperature.

3. FIELDS OBSERVED

The observed sample of CO hotspots is comprised of two parts; i) observations of gas within 5-

30' of the positions of compact extragalactic continuum sources used to study molecular absorption at radio wavelengths, and ii) observations over a region of extent 90' toward the translucent cloud L121 southwest of the star ζ Oph. Except for the continuum source B0528-134 that is observed through the Eridanus Loop, the gas seen around the continuum background sources is well removed from regions showing $A_V \gtrsim 1$ mag. As shown in Figure 1 of Liszt & Pety (2012), B0954+658 ($E_{B-V} = 0.12$ mag) and B2251+158 ($E_{B-V} = 0.10$ mag) are within a few degrees of MBM 23 and MBM 55 (Magnani et al. 1985) having $E_{B-V} = 0.13$ and 0.29 mag, respectively. B1954+513 ($E_{B-V} = 0.15$ mag) and B0736+017 ($E_{B-V} = 0.13$ mag) are more isolated. The material studied here samples the diffuse, occasionally partially-

molecular ISM that is broadly distributed outside dark/molecular cloud complexes.

By contrast, L121 in Ophiuchus is only 1° - 2° removed from a very extended optically-opaque filament L204 whose CO emission is redshifted by some 4 km s^{-1} , as shown in Fig. 1 of Liszt et al. (2009). The fact that L121 and L204 had such comparable CO brightnesses was a strong motivating factor for this work.

3.1. Four fields around compact mm-wave continuum sources

Figure 1 shows results for CO and ^{13}CO around the positions of four extragalactic continuum sources. In the center column are cut-outs of the larger CO maps shown in Liszt & Pety (2012) with peak positions and the location of the continuum marked by crosses. The peak integrated brightness of the ^{12}CO emission is shown at the top of the color bar scale at the right side of each map: these vary from $4\text{-}7 \text{ K-km s}^{-1}$. To either side, profiles taken toward the continuum or at the nearby peaks are shown, with connecting lines drawn between the positions of CO peaks and the boxes containing the profiles observed there. As noted in the earlier work, CO lines have typical brightness $1\text{-}2 \text{ K}$ toward the continuum, and CO peaks of remarkably similar brightness $4\text{-}5 \text{ K}$ nearby. ^{13}CO is detected at most of the positions and is remarkably bright toward the western, blue-shifted CO peak near B1954+513. This was by chance the very first position observed in ^{13}CO in the course of this work. However similar the CO brightnesses of the peaks may be around B1954+513, the ^{13}CO brightness varies by more than a factor 5.

3.2. The field around B0528+134

A more extensive set of observations around B0528+134 is shown in Figure 2. In the center are four map panels representing ^{13}CO emission at top and ^{12}CO below, each species sampled over two velocity ranges corresponding to the blue-shifted gas around 1.75 km s^{-1} at left and the redshifted component at $9\text{-}12 \text{ km s}^{-1}$ at right. Connecting

lines are drawn between map locations and the boxes containing the spectra there, and the same position is sometimes represented by two boxes with different contents and/or scaling of the brightness.

The line of sight to B0528+134 passes near the Eridanus Loop and is not characterized by especially small extinction; $E_{B-V} = 0.89 \text{ mag}$ in Table 1. However, the HCO^+ column density measured in absorption is smaller than that seen toward BL Lac at $E_{B-V} = 0.32 \text{ mag}$, indicating locally diffuse conditions. The CO emission pattern around B0528+134 is characterized by very regular striations of a component at $9\text{-}12 \text{ km s}^{-1}$ having high contrast and very high CO peak brightnesses typically near 10 K , shown over a wider field by Liszt & Pety (2012). This may be the second example of a phenomenon originally seen in Orion (Berné et al. 2010) and ascribed to “waves” at the surface of the Orion molecular cloud, near where massive stars are forming.” Alternatively, striations in molecular gas are discussed by (Heyer et al. 2016) and (Tritsis et al. 2018) and ascribed to some combination of instability, MHD waves and alignment with the magnetic field.

As shown in the CO maps in the lower row at the center in Figure 2, the blue-shifted component overlaps a limited portion of the red-shifted emission to the southeast of the continuum and is absent elsewhere. This similarity of morphology suggests a physical connection but the conditions in the red and blue-shifted gas are dissimilar. Comparing the upper and lower maps in either column, one sees that the blue-shifted gas in the left-hand column is much fainter in ^{13}CO . Observations at the position B0528T shown in boxes at the lower left corner of Figure 2 illustrate the complexity of the variation in the line brightnesses. At a position where both the red and blue components are equally bright in ^{12}CO the red peak is much brighter in ^{13}CO . To the blue where ^{13}CO is weaker, ^{13}CO , HCO^+ and CS are all about equally bright. To the red, ^{13}CO is

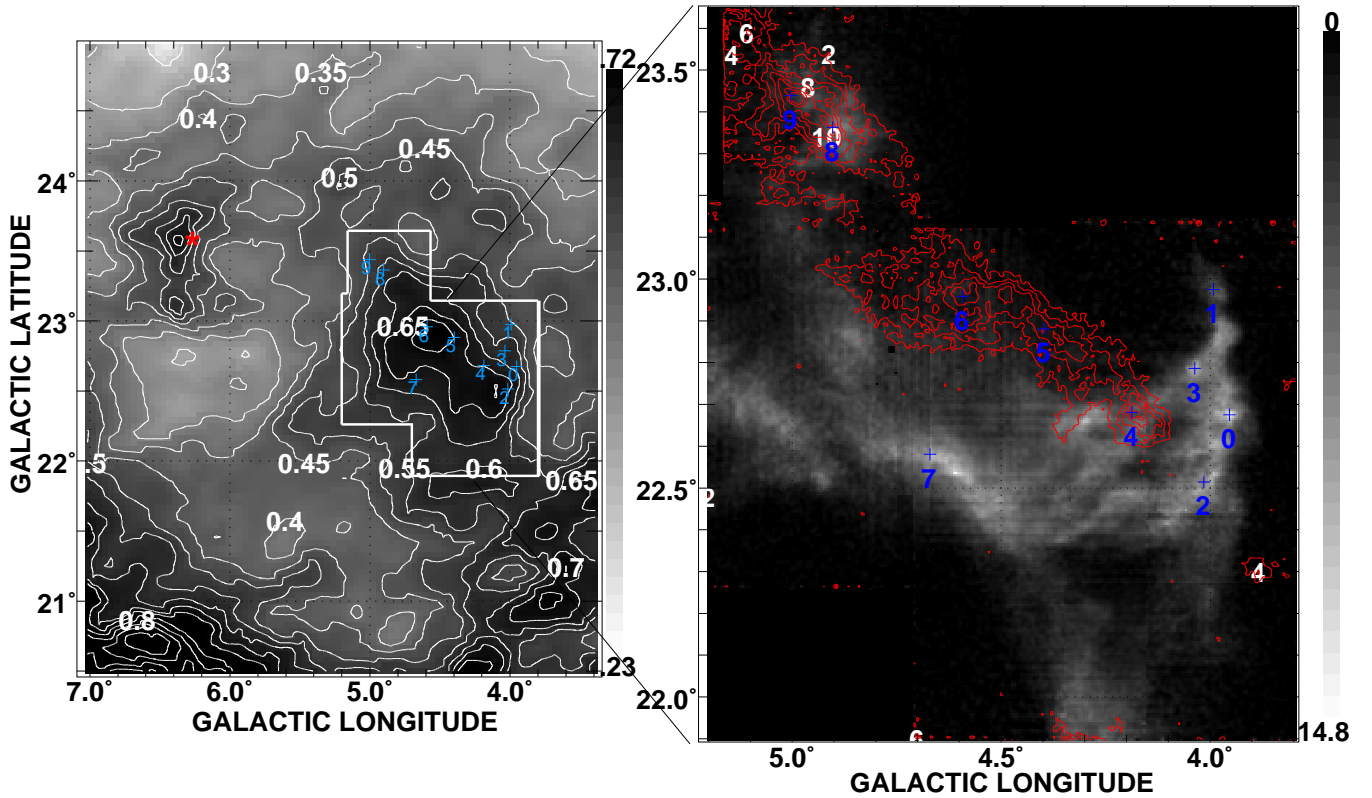


Figure 4. Reddening and CO emission in the vicinity of ζ Oph, L121 and L204 (Liszt et al. 2009). Left side panel: A map of E_{B-V} Schlegel et al. (1998) with contours in steps of 0.05 mag and a gray scale running from 0.23 to 0.72 mag as indicated on the adjacent bar scale. The position of the star ζ Oph is marked by a red asterisk and the portion of L121 mapped in ^{12}CO emission at the ARO 12m at $1'$ spatial resolution is outlined. Indicated in blue in both panels are 10 labelled locations Z0..Z9 ordered in galactic longitude where additional pointed observations with higher spectral resolution were taken (see Figure 5 and Table A1). A small part of the filamentary cloud L204 is visible as the high extinction region at lower left. Right side panel: ARO ^{12}CO maps of CO emission from L121 at $1'$ resolution on an expanded spatial scale. This panel is a composite of a gray scale representation of integrated emission at $v < -0.7$ km s^{-1} with peak $W_{\text{CO}} = 14.8$ K km s^{-1} , and contours in red at levels 2, 4, .. 14 K km s^{-1} representing the integrated emission at $v > -0.7$ km s^{-1} .

an order of magnitude brighter than HCO^+ and CS is not detected. Variations in the HCO^+/CS brightness ratio are indicative of large differences in their relative abundances as discussed by Liszt (2012) and in more detail in Section 5.2.

3.3. The field around BL Lac

Figure 3 shows profiles at four positions near BL Lac, as marked on a cutout of the ^{12}CO map shown in Liszt & Pety (2012). Profiles of ^{12}CO scaled downward by a factor of 30 are shown as grey histograms with profiles of HCO^+ J=1-0 in red and CS J=2-1 in blue and dashed. Unlike most of the other directions observed here, ie the posi-

tions sampled around B0528-134 in Figure 2 (see Section 5.2), HCO^+ and CS emission have comparable brightness at all four locations. ^{13}CO observations at these positions were thwarted when a snowstorm bore down on the mountain on the day of the Newtown School shootings in December 2012 during the final observing run of this program. The peak integrated brightness of the ^{12}CO emission is 21 K-km s^{-1} , which seems remarkable given that the peak reddening is $E_{B-V} = 0.36$ mag in this region (Liszt & Pety 2012).

3.4. L121

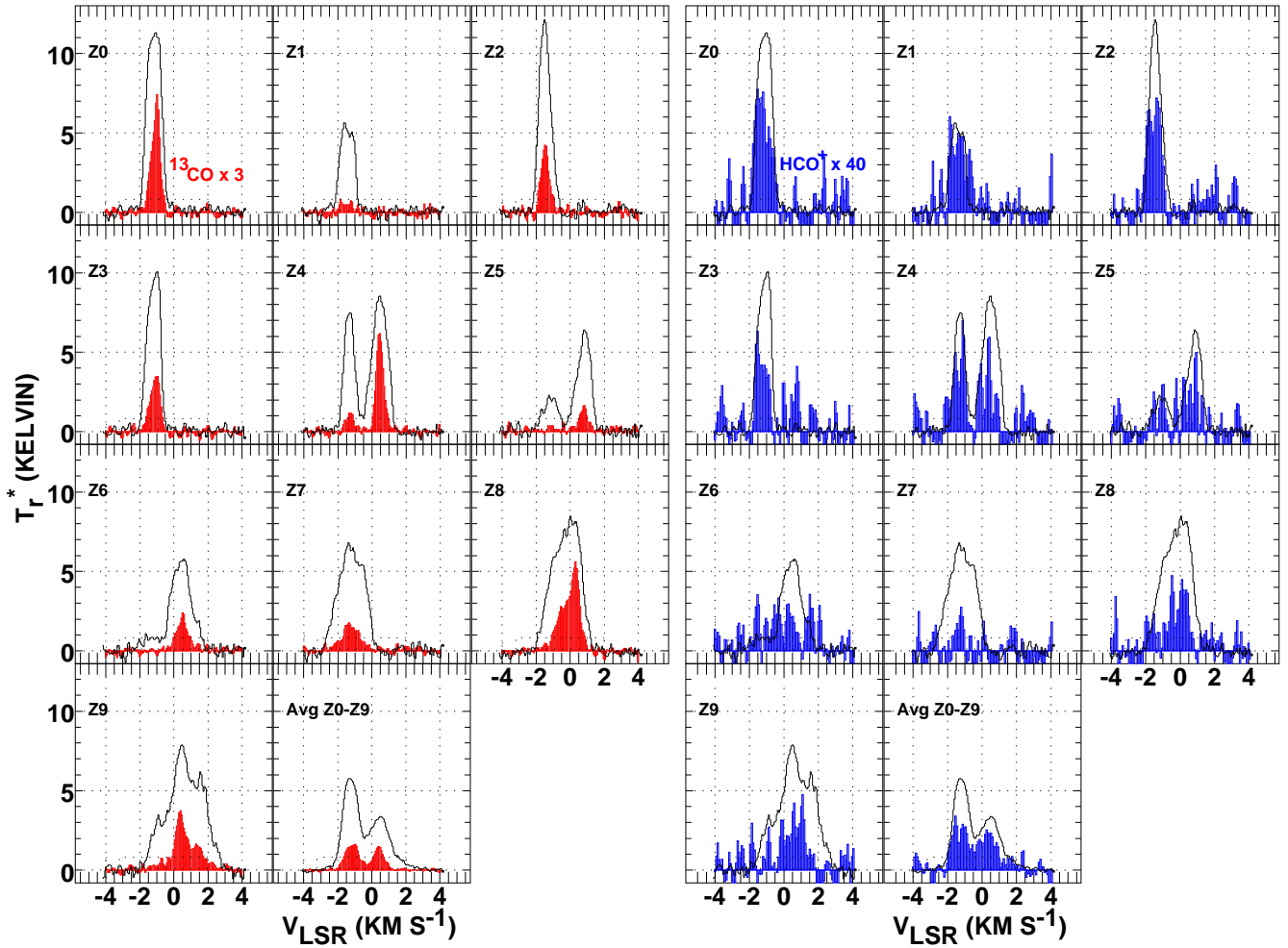


Figure 5. ^{12}CO , ^{13}CO , and HCO^+ emission from 10 pointings in L121 and their unweighted average at bottom right in each panel. At left ^{13}CO emission scaled upward by a factor 3 is shown in red overlaid on CO, while at right HCO^+ shown in blue and scaled upward by a factor 40 is overlaid on CO.

Figure 4 gives an overview of the observing done in the L121 region near ζ Oph (Liszt et al. 2009). At left is a map of reddening E_{B-V} using the data of Schlegel et al. (1998) with the star marked by a red asterisk to the northeast. The minimum reddening 0.23 mag must largely be associated with foreground and background material: The material associated with L121 contributes about $0.65 - 0.23 = 0.4$ mag of reddening, or some 1.2 magnitudes of visual extinction in a region where the peak reddening $E_{B-V} = 0.65$ mag indicates 2 magnitudes of visual extinction.

CO was mapped over the region outlined at left in Figure 4 by stitching together numerous OTF tiles of size approximately $30' \times 30'$. The grey scale at

right with a peak of $W_{\text{CO}} = 15 \text{ K-km s}^{-1}$ represents the integrated CO profile of the blue-shifted CO emission at $v \leq -0.7 \text{ km s}^{-1}$: the contours in red are for the red-shifted emission at $v > -0.7 \text{ km s}^{-1}$ that is rather distinct from the more blue-shifted emission. Both components are observed in optical absorption and radiofrequency emission toward the star ζ Oph itself. Numbers in white in the right-side frame in Figure 4 are the integrated brightness of the red-shifted emission which peaks just above 10 K-km s^{-1} to the north.

Indicated at left and right in Figure 4 are ten locations labeled 0..9 in order of increasing galactic longitude at which pointed observations of CO, ^{13}CO and HCO^+ were taken, as shown in part in

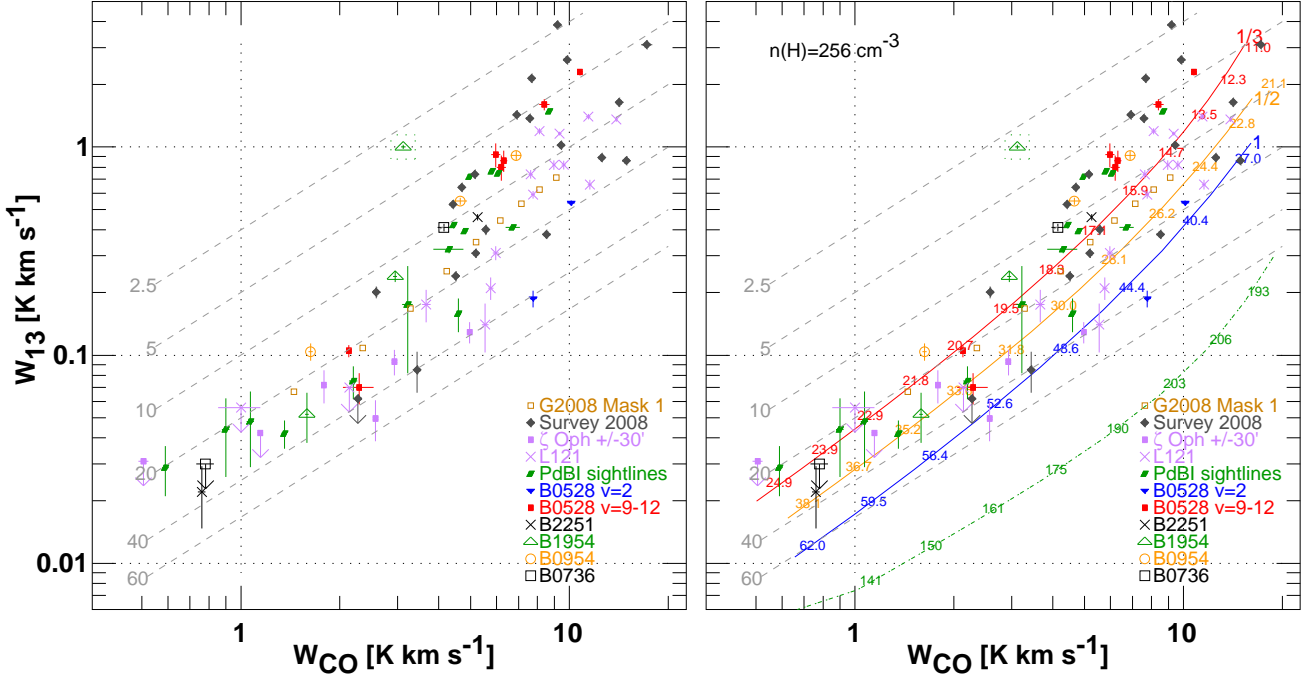


Figure 6. ^{13}CO and ^{12}CO emission for various datasets. Fiducial values of the W_{CO}/W_{13} ratio are shown as grey dashed lines. Right: with model results superposed for $n(\text{H}) = 256 \text{ cm}^{-3}$ and three scaled strengths of the illuminating radiation field, at full, one-half and one-third strength ($G_0 = 1, 1/2,$ and $1/3$ respectively). Results neglecting isotope exchange for $G_0 = 1$ are shown as a green dash-dotted line. The numbers along the model curves are the $N(\text{CO})/N(^{13}\text{CO})$ column density in the model, for comparison with the intensity ratio that is plotted. In general the brightness and column density ratios track each other even when they are much smaller than the inherent isotopic abundance ratio of $\text{C}/^{13}\text{C} = 62$.

Figure 5. Positions 0 and 9 were observed in C^{18}O and a few positions were also observed in CS. CO, ^{13}CO and HCO^+ profiles toward the 10 enumerated positions and their unweighted mean are shown in Figure 5. At left, ^{13}CO profiles scaled upward by a factor three are overlaid on ^{12}CO . At right, HCO^+ profiles scaled upward by a factor 40 are overlaid on ^{12}CO . As with the other fields, CO components with similar W_{CO} have widely varying ^{13}CO brightness.

4. RESULTS FOR CO ISOTOPOLOGUES

4.1. C^{13}O and ^{12}CO

Figure 6 shows a summary of the new and existing observations of CO and ^{13}CO in diffuse molecular gas: the new data discussed here have been added to the comparable Figure 4 in Liszt (2017). The brightest ^{12}CO lines in diffuse/translucent gas generally have $W_{\text{CO}} \approx 10 \text{ K-km s}^{-1}$ corresponding

to $N(\text{CO}) \approx 10^{16} \text{ cm}^{-2}$. Exceptions occur in the larger field around BL Lac (Figure 3), toward L121 when the CO line is broad and the red and blue shifted components cannot be separated (Table 2 and Figure 5), and for a few sightlines toward stars used as UV absorption line targets. Many of the smallest ratios $W_{\text{CO}}/W_{13} < 5$ and the largest W_{CO} values arise along sightlines toward UV absorption line targets, in which case CO emission likely originates from dense placental material situated behind the stellar targets: stars seen behind gas emitting very bright CO lines would likely have been too heavily extinguished to serve as good UV absorption line targets.

With the notable exception of one datapoint with very strong ^{13}CO emission near B1954+513 (Figure 1), the diverse observational samples provide a consistent overall picture whereby $W_{13}/W_{\text{CO}} \approx$

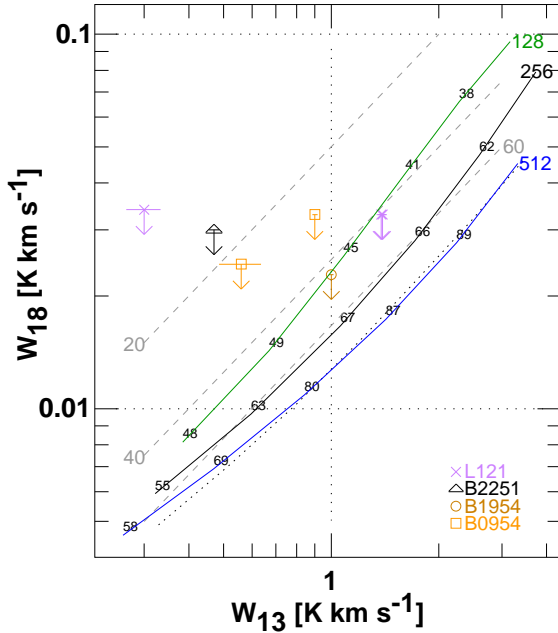


Figure 7. Observed and calculated C^{18}O and ^{13}CO emission profile integrals. Fiducial values of the ratio $W_{13}/W_{18} = 20, 40$ and 60 are shown as grey dashed lines. Also shown are calculated brightnesses for $n(\text{H}) = 128$ (green), 256 (black) and 512 (blue) cm^{-3} at full strength and as a dotted black line for $n(\text{H}) = 256 \text{ cm}^{-3}$ with the radiation field at half-strength, showing that the brightness ratio scales as $G_0/n(\text{H})$. Numbers along the curves indicate the intrinsic $N(^{13}\text{CO})/N(\text{C}^{18}\text{O})$ ratio. The intrinsic $^{13}\text{C}/^{18}\text{O}$ ratio in the gas is $520/62 = 8.4$.

$1/40 - 1/20$ at $W_{\text{CO}} \lesssim 4 \text{ K-km s}^{-1}$, increasing so that $W_{13}/W_{\text{CO}} \approx 1/20 - 1/5$ at $W_{\text{CO}} \gtrsim 4 \text{ K-km s}^{-1}$.

To understand the observations we show at right in Figure 6 the same data with model results for gas of total density $n(\text{H}) = 256 \text{ cm}^{-3}$ and three values of the scaled strength of the incident radiation field $G_0 = 1, 1/2$ and $1/3$: the underlying assumptions and methods of the models are discussed in Section 2.3. Along each model curve there are numbers representing the ratio of column densities $N(^{12}\text{CO})/N(^{13}\text{CO})$ in the model. These can be compared with the intensity ratios in the plot to assess the degree to which the CO column densities and emission brightnesses track each other, as stressed in Liszt (2017). To aid in this comparison,

fiducial lines are shown at fixed intensity ratios 20, 40 and 60.

In the righthand panel in Figure 6 the lowest-lying model curve shows results when the carbon isotope exchange is ignored: Clearly, the success of the models depends most nearly on this process, and very nearly all of the observed ^{13}CO is formed from the reaction of $^{13}\text{C}^+$ with ^{12}CO , not from the recombination of H^{13}CO^+ with electrons. A comparable situation arises for HD that is almost entirely formed *in situ* in the gas through gas-phase exchange reactions of deuterium and hydrogen (Liszt 2015) although, in that case, HD is largely self-shielding (Le Petit et al. 2002).

The effects of changing the density and radiation field are complex in models where the heating is largely through the photoelectric effect on small grains, from photons of about the same energy as those that ionize carbon and photodissociate H_2 and CO. Slower photodissociation and lower kinetic temperature each encourage more effective carbon isotope exchange while lower temperatures cause faster recombination of HCO^+ to CO, weakening the fractionation while allowing a given $N(\text{CO})$ to form at lower $n(\text{H})$, $N(\text{H})$ and $N(\text{H}_2)$. At a given W_{CO} the W_{13}/W_{CO} integrated brightness ratio increases with higher density and weaker illumination, with a progressively stronger density dependence at smaller values of G_0 . The highest observed values of W_{13}/W_{CO} require some combination of higher density and weaker radiation and the effect of dimming the radiation is stronger at the higher densities.

For $W_{\text{CO}} \lesssim 4 \text{ K-km s}^{-1}$ where $W_{13}/W_{\text{CO}} \approx 1/40 - 1/20$ the data can generally be explained at any number density $n(\text{H}) \gtrsim 128 \text{ cm}^{-3}$, but even the lowest of these densities is already large enough that the molecular fraction $\langle f_{\text{H}_2} \rangle = 2N(\text{H}_2)/N(\text{H}) \gtrsim 0.7$ according to Figure 6 of Liszt (2017).

The isotopologic intensity ratio W_{CO}/W_{13} tracks the column density ratio $N(\text{CO})/N(^{13}\text{CO})$ even when both ratios are much less than 62 and the proportionality between brightness and column den-

sity persists well beyond the domain where $\tau > 1$ as long as the excitation is strongly sub-thermal (Goldreich & Kwan 1974). The difference between W_{CO}/W_{13} and $N(\text{CO})/N(^{13}\text{CO})$ is about 20% at $W_{\text{CO}} = 5 \text{ K-km s}^{-1}$ or 40% at $W_{\text{CO}} = 10 \text{ K-km s}^{-1}$, with slightly larger differences at smaller G_0 . The point is that when the isotopologic brightness ratio significantly departs from 62, the actual abundance ratio is much closer to the observed brightness ratio than to the intrinsic isotopic abundance ratio. $N(^{12}\text{CO})$ cannot be reliably estimated from comparing the ^{12}CO and ^{13}CO brightnesses under the common assumption that both isotopologues are present in the intrinsic ratio, and the wide variations in $N(\text{CO})/N(\text{H}_2)$ in any case mean that $N(\text{CO})$ cannot be used to infer $N(\text{H}_2)$ in any case. This point was stressed by Szucs et al. (2016) who concluded that it was more accurate to derive $N(\text{H}_2)$ by scaling W_{CO} with a CO- H_2 conversion factor. If desired, the carbon monoxide column densities can be estimated as $N(\text{CO}) = 10^{15} \text{ cm}^{-2} W_{\text{CO}}$ and similarly for other isotopologues.

Two aspects of the data in Figure 6 deserve comment insofar as they relate to a comparison with UV absorption line data as discussed by (Liszt 2017). The nearly constant ratio $N(\text{CO})/N(^{13}\text{CO}) \approx 65$ seen in UV absorption at $N(\text{CO}) < 10^{16} \text{ cm}^{-2}$ is higher than that inferred from mm-wave emission brightness ratios and corresponds most closely to the curves for $G_0 = 1$: The gas observed in optical absorption is mostly unfractionated, from which we infer that it is subject to a stronger radiation field and is warmer and less dense than that observed in mm-wave emission. Conversely, the CO emission data taken in directions toward the same early-type stars that are observed in UV absorption (Liszt 2008) require a diminished radiation field at the density $n(\text{H}) = 256 \text{ cm}^{-3}$ that was used in Figure 6. The counter-intuitive inference of a weaker radiation field is consistent with the notion that strong CO emission toward the absorption line stars arises in dense fully-molecular gas behind the star because these

stars would not have been suitable UV absorption targets with the opposite geometry. ζ Oph is a case where little or none of the molecular emission observed in its direction arises behind the star, but the emission is weak, $W_{\text{CO}} \approx 1 \text{ K-km s}^{-1}$.

4.2. C^{18}O

Few measurements of absorption by C^{18}O are available in the UV, but two sightlines with $N(\text{CO}) = 2 \times 10^{15} \text{ cm}^{-2}$ and $= 2.5 \times 10^{16} \text{ cm}^{-2}$ show C^{18}O depletions of 3 and 6, respectively, with respect to the ratio $N(\text{CO})/N(\text{C}^{18}\text{O}) = 520$ (see Figure 1 of (Liszt 2017)). The mm-wave measurements presumably sample gas with weaker radiation fields and weaker selective photodissociation of C^{18}O .

Figure 7 shows the limited amount of meaningful data we have been able to gather on the integrated intensity of C^{18}O , W_{18} , compared with W_{13} . Also shown in Figure 7 are calculated brightnesses for $n(\text{H}) = 128, 256$ and 512 cm^{-3} with the radiation field at full strength and at $n(\text{H}) = 256 \text{ cm}^{-3}$ with $G_0 = 1/2$. Given along the curves showing model results are the intrinsic $N(^{13}\text{CO})/N(\text{C}^{18}\text{O})$ ratios: these can be compared with the model brightness ratios to see that the observed brightness ratios can straightforwardly be interpreted as column density ratios. The model brightnesses are weakly dependent on G_0 and $n(\text{H})$ in opposite senses, falling with G_0 , and the model brightness ratio scales approximately as $G_0/n(\text{H})$ (the curves coincide for $n(\text{H})=512 \text{ cm}^{-3}$, $G_0=1$ and $n(\text{H})=256 \text{ cm}^{-3}$, $G_0=1/2$).

C^{18}O emission is very weak in diffuse molecular gas, with 3σ observational upper limits $W_{13}/W_{18} > 25 - 40$ in several cases as against an intrinsic isotopic abundance ratio $^{13}\text{C}/^{18}\text{O} = 520/62 = 8.4$. If $N(^{13}\text{CO})$ is enhanced by a factor g , the implied C^{18}O depletion factors are $(25-40)/8.4/g = (3-5)/g$. The limited range of relatively large W_{13} values sampled in Figure 7 corresponds to high values $g \gtrsim 2 - 4$ (see Figure 6) so the mm-wave measurements disappointingly do not constrain the C^{18}O depletion at the levels observed in UV absorption spectra.

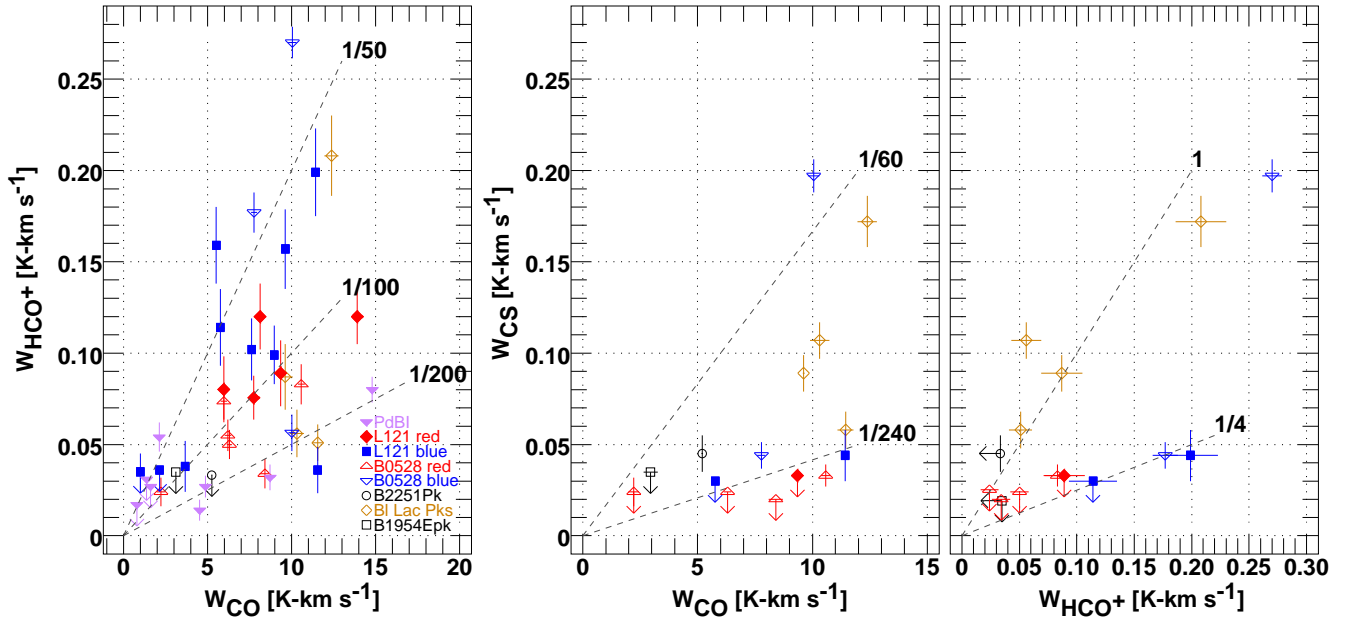


Figure 8. Observed ^{12}CO , HCO^+ , and CS profile integrals. Fiducial values are shown as grey dashed lines.

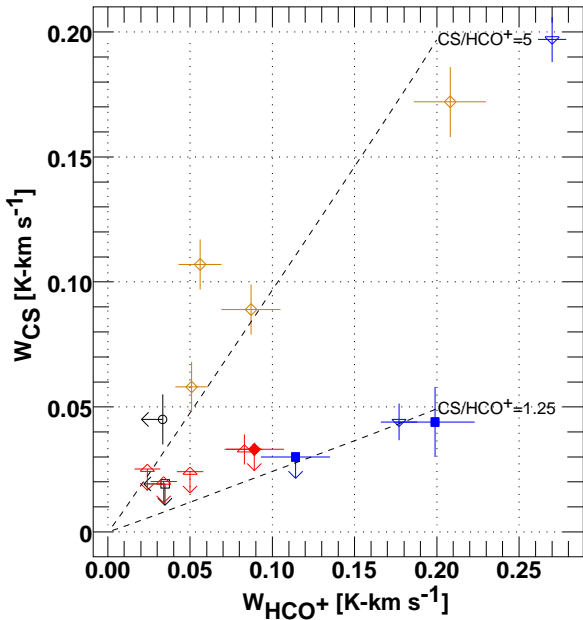


Figure 9. As in the right-most panel of Figure 8, but with model results for two values of the abundance ratio, $\text{CS}/\text{HCO}^+ = 5$ and $5/4$. Calculated results are not perceptibly different for different density $n(\text{H})$ and illumination G_0 .

5. EMISSION FROM STRONGLY-POLAR SPECIES HCO^+ AND CS

Figure 8 summarizes the HCO^+ and CS $J=2-1$ observations with respect to each other and with

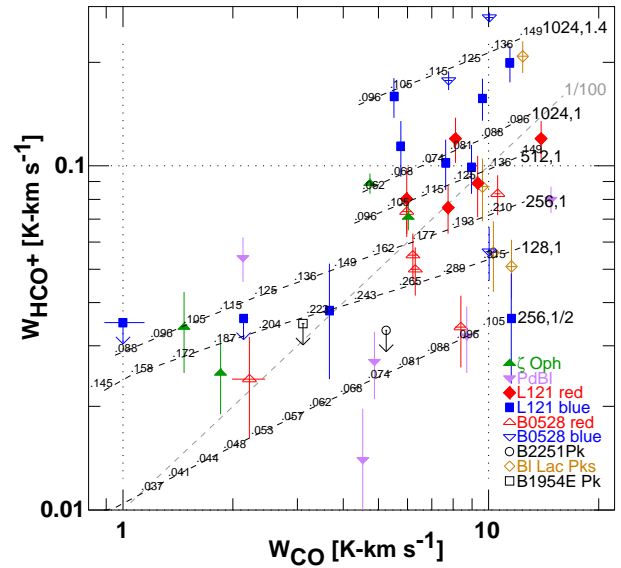


Figure 10. Observed ^{12}CO and HCO^+ line profile integrals on a logarithmic scale with model results. Labels at the right hand side of each model curve represent $n(\text{H})$ in units of cm^{-3} and the radiation field scaling parameter G_0 . Numbers along the model curves are the reddening E_{B-V} . A fiducial line with $W_{\text{HCO}^+}/W_{\text{CO}} = 0.01$ is shown grayed and dashed.

respect to CO. The panel plotting W_{HCO^+} vs. W_{CO} at left shows that HCO^+ brightens considerably for $W_{\text{CO}} = 6 - 10 \text{ K-km s}^{-1}$ but $W_{\text{HCO}^+}/W_{\text{CO}} = 1/200 - 1/50$ quite generally. Such ratios are characteris-

tic of gas in the disk of the inner Milky Way, outside the galactic center (Liszt 1995; Helfer & Blitz 1997), and other galaxies (Jiménez-Donaire et al. 2019) as discussed in Section 6.8.

CS J=2-1 emission brightens abruptly at $W_{\text{CO}} \gtrsim 10 \text{ K-km s}^{-1}$ in the middle panel of Figure 8, from data in the blue component around B0528 (see Figure 2) and around BL Lac (Figure 3). The right-most panel in Figure 8 shows that the $W_{\text{CS}}/W_{\text{HCO}^+}$ ratio is bimodal. The same datapoints toward BL Lac and in the blue component around B0528 having stronger CS emission at $W_{\text{CO}} = 10\text{-}12 \text{ K-km s}^{-1}$ in the middle panel have three-four times larger $W_{\text{CS}}/W_{\text{HCO}^+}$ ratios than the rest of the data, over a wide range of W_{HCO^+} .

The HCO^+ J=1-0 and CS J=2-1 line brightnesses are small enough that both are in the weak excitation limit of Liszt & Pety (2016) and the line profile integral may be expressed as a line of sight integral through the emitting medium

$$\int T_B dv = (\lambda^2/8 \times 10^5 \pi)(hc/k) \int n(\text{H})\gamma_u n(\text{Y})dL \quad (1)$$

where Y stands for HCO^+ or CS and γ_u is an excitation rate per H-nucleus determined by the local temperature and ionization fraction. The emergent line brightness is roughly proportional to the product of the mean number density of hydrogen and the column density of the emitting molecule, not its critical density. Details of the cloud structure and molecular abundance distribution are washed out by the line of sight integration and the emergent line brightnesses are not explicitly dependent on the optical depth.

5.1. $W_{\text{CS}}/W_{\text{HCO}^+}$ and $N(\text{CS})/N(\text{HCO}^+)$ are bimodal

The bimodality of the $W_{\text{CS}}/W_{\text{HCO}^+}$ brightness ratio in the right-most panel of Figure 8, with values approximately 1 and 1/4, reflects a real bimodality of the $N(\text{CS})/N(\text{HCO}^+)$ abundance ratio: there is no effect associated with the excitation that can cause such a difference given that both species

must coexist in the regions that have higher H_2 fractions. Shown in Figure 9 are results for the model brightnesses of CS J=2-1 and HCO^+ under the assumption that $n(\text{CS})/n(\text{HCO}^+) = 5$ and $n(\text{CS})/n(\text{HCO}^+) = 5/4$ everywhere in the models (recall that $n(\text{HCO}^+)/n(\text{H}_2) = 3 \times 10^{-9}$ is fixed while $n(\text{H})$ and $n(\text{H}_2)$ vary) and the model results for the intensity ratio are insensitive to $n(\text{H})$.

As discussed in Appendix C, bimodality of the $N(\text{CS})/N(\text{HCO}^+)$ ratio was not observed in our survey of mm-wave HCO^+ and CS absorption (Lucas & Liszt 2002), because the sight-lines directly toward continuum sources sample material with CO emission well below the W_{CO} values where bimodality is evident in Figure 8. The previously-observed column density ratios $N(\text{CS})/N(\text{HCO}^+)$ derived in absorption have mean $\langle N(\text{CS}) \rangle / \langle N(\text{HCO}^+) \rangle = 1.27$ and $\langle N(\text{CS}) \rangle / \langle N(\text{HCO}^+) \rangle = 1.66 \pm 1.32$ and are in overall agreement with the column density ratios derived now in emission alone.

Bistability is a recognized phenomenon in chemical networks for dense gas (Le Bourlot et al. 1993; Lee et al. 1998; Charnley & Markwick 2003; Boger & Sternberg 2006; Wakelam et al. 2006; Dufour & Charnley 2019) and the abundance of CS is one of the earliest recognized markers (Le Bourlot et al. 1993). Gerin et al. (1997) found a column density of CS in a core in Polaris at $E_{\text{B-V}} \approx 0.6 \text{ mag}$ that was 20-40 times higher than in Taurus at $E_{\text{B-V}} \gtrsim 1 \text{ mag}$: the $N(\text{CS})/N(\text{HCO}^+)$ ratio was about a factor two higher in Polaris even as the brightness ratio $W_{\text{CS}}/W_{\text{HCO}^+}$ was smaller by a factor three, being 2 in Taurus and 0.7 in Polaris. The kind of bistability that is discussed for dense gas chemical networks with a contrast between high and low ionization phases driving changes in the abundance of H_3^+ is not obviously relevant in diffuse molecular gas where CO is a minority constituent, the ionization fraction is high and electron recombination of H_3^+ is rapid.

5.2. HCO^+ and CO

On its own terms the HCO^+ line brightness is subject to the same considerations of the weak excitation limit as CS, but the special role of HCO^+ as the progenitor of CO and its fixed abundance with respect to H_2 mean that the comparison of W_{CO} and W_{HCO^+} has broader implications for the CO formation chemistry.

As a first approach to interpret the HCO^+ data with respect to CO, recall that the rotational excitation of HCO^+ is dominated by collisions with electrons in diffuse molecular gas (Liszt 2012; Liszt & Pety 2016) where $n(e)/n(\text{H}) \approx 2 - 3 \times 10^{-4}$ as the result of photoionization of carbon and a somewhat smaller contribution from cosmic-ray ionization of atomic hydrogen (Draine 2011). The electron abundance declines at higher density as the H^+ fraction decreases but $n(e)$ remains high until C^+ recombines to CO (Liszt 2011). In this case $W_{\text{HCO}^+} \propto \int n(\text{H})n(\text{HCO}^+)dL \propto \int n(e)n(\text{HCO}^+)dL$. However, CO is formed from the thermal recombination of HCO^+ with electrons so W_{HCO^+} is also proportional to the column-averaged CO formation rate. With $W_{\text{CO}} \propto N(\text{CO})$, the $W_{\text{HCO}^+}/W_{\text{CO}}$ brightness ratio is equivalent to taking the ratio of the column-averaged CO formation rate to the resulting CO column density. When this is larger, a higher formation rate is being required to produce a given amount of CO, so the destruction rate must be larger. Viewed in this way, the variation in W_{HCO^+} at $W_{\text{CO}} = 6\text{-}12 \text{ K-km s}^{-1}$ in the leftmost panel of Figure 8 suggests a wide range in CO photodestruction rates.

Viewed another way, $W_{\text{HCO}^+}/W_{\text{CO}} \propto \langle n(\text{H}) \rangle N(\text{HCO}^+)/W_{\text{CO}} \propto \langle n(\text{H}) \rangle N(\text{H}_2)/N(\text{CO})$, so the $W_{\text{HCO}^+}/W_{\text{CO}}$ brightness ratio also samples the relative CO abundance, testing whether the observed CO emission is being produced at reasonable $n(\text{H})$ and $N(\text{H}_2)$. The low-light models that fractionate CO more readily in the right-hand panel of Figure 6 will produce a given $N(\text{CO})$ and W_{CO} at smaller $N(\text{H}_2)$, and so with weaker HCO^+ emission.

These two viewpoints are illustrated with calculations of the $W_{\text{HCO}^+}/W_{\text{CO}}$ brightness ratio in Figure 10, again showing the data from the left-most panel of Figure 8, but on logarithmic scales. The models with $G_0 = 1$ run through the base level of HCO^+ emission with a relatively weak density dependence that confirms the consistency of the overall CO formation scheme based on recombination of the observed relative abundance of HCO^+ . The models reproduce the observed HCO^+ brightness and CO column density at typical values of the molecular hydrogen column density. The data toward L121 in the field of ζ Oph are reproduced with a stronger radiation field and a higher density, along with two of the three datapoints in the blue component of B0528 and one point in the field around BL Lac.

With the weaker illumination needed to enhance ^{13}CO there is little density dependence in the model $W_{\text{HCO}^+}/W_{\text{CO}}$ ratios and one curve is plotted for $n(\text{H}) = 256 \text{ cm}^{-3}$ covering the density range $n(\text{H}) = 128 - 512 \text{ cm}^{-3}$ at $G_0 = 1/2$: the reddening values given along the relevant curve scale inversely with $n(\text{H})$. As indicated in Figure 10, and as expected, the low-light models produce a given $N(\text{CO})$ or W_{CO} at much smaller $N(\text{H})$ and $E_{\text{B-V}}$, and with W_{HCO^+} weaker by about a factor two compared to the models with fuller illumination. The low-light conditions that reproduce $N(\text{CO})$, W_{CO} and $N(^{13}\text{CO})$ at $W_{\text{CO}} \lesssim 5 \text{ K-km s}^{-1}$ account for only about one half of the base level of HCO^+ emission $W_{\text{HCO}^+} \approx 0.02 - 0.03 \text{ K-km s}^{-1}$ at $W_{\text{CO}} \lesssim 5 \text{ K-km s}^{-1}$ but with correspondingly smaller total column density and $E_{\text{B-V}}$.

The CO hotspots near the mm-wave continuum background sources are explained as embedded, localized regions perhaps with higher density, but even more likely with increased shielding, occupying a small fraction of the volume of the overall diffuse molecular medium. In turn, much or most of the HCO^+ emission arises in other material that makes a small contribution to the CO abundance and emission.

5.3. CO hotspots near mm-wave background sources

Enhanced and faster formation of H₂ and CO in localized regions of greater density and optical shielding are common features of turbulent models of the HI→H₂ transition in diffuse molecular gas (Shetty et al. 2011; Godard et al. 2014; Valdivia et al. 2017; Bialy et al. 2019). Most likely the CO hotspots observed near the background mm-wave continuum sources and shown in Figure 1 are examples of this phenomenon. The similarity of the sizes (10′) and peak brightnesses (5 K-km s⁻¹) of the hotspots seen in the vicinity of the mm-wave background sources in Figure 1 suggest that common physical phenomena and physical conditions are being sampled. The extraordinarily small W_{CO}/W₁₃ ratio (3:1) observed toward the West peak around B1954+513 is in marked contrast to the much larger values, typically 20:1, seen in the other directions. This requires further investigation.

As a specific example, consider that the low-light models with n(H) = 256 cm⁻² shown in Figure 10 are at most about 80% molecular, ie n(H₂) ≲ 100 cm⁻², and produce 1 K-km s⁻¹ ≤ W_{CO} ≤ 5 K-km s⁻¹ at 0.04 ≲ E_{B-V} ≲ 0.07 mag. With N(H)/E_{B-V} ≈ 8 × 10²¹ cm⁻²(mag)⁻¹ (Liszt 2014a,b; Hensley & Draine 2017) and [C]/[H] = 1.6 × 10⁻⁴ (Sofia et al. 2004), one would expect N(C⁺) = 5.3–9.3 × 10¹⁶ cm⁻². Because the required CO column densities are 1 – 5 × 10¹⁵ cm⁻² there is ample margin for N(CO) to increase, and CO emission to brighten to levels W_{CO} = 5 K-km s⁻¹, without upsetting the balance of the carbon ionization equilibrium that maintains the preponderance of carbon in C⁺. At a nominal distance of 250 pc as for the field around B2251+158 (Zucker et al. 2019), a region with E_{B-V} = 0.05 mag and n(H) = 256 cm⁻² has a size N(H)/n(H) = 4 × 10²⁰ cm⁻²/256 cm⁻³ = 0.51 pc, subtending an angular size 8.0′. This is a typical size for the regions of enhanced CO emission in Figure 1.

The required N(H) and E_{B-V} scale inversely with the density, so the implied angular size would vary approximately as 1/n(H)². The surrounding medium could be an order or magnitude more expansive with a factor ≳ 3 density contrast that would suffice to lower the molecular fraction and substantially weaken the CO emission (Liszt 2017). These scalings are important to understanding the presence of the CO hotspots along lightly-reddened sightlines, in the absence of evidence for variations in the reddening comparable to the contrasts in W_{CO}. It is not necessary to imagine a contraction of the entire medium into clumps as small as the CO emission regions shown in Figure 1.

6. SUMMARY AND DISCUSSION

6.1. ¹²CO and ¹³CO

Once upon a time we mapped ¹²CO emission around the locations of a dozen extragalactic mm-wave background continuum sources that had been used to survey for the presence of molecular gas by observing the J=1-0 line of HCO⁺ in absorption. We noted the presence of quite strong peak profile-integrated CO J=1-0 emission W_{CO} ≳ 5 K-km s⁻¹ in regions of very modest reddening E_{B-V} = 0.1 - 0.3 mag (our CO “hotspots”) when only much weaker CO emission had been seen a few arcminutes away toward the continuum sources themselves.

In this work we followed up by observing ¹³CO, C¹⁸O, HCO⁺ and CS J=2-1 emission at positions of strong CO emission in five of these previously-studied regions and we mapped a more extended portion of the L121 cloud south of the bright star ζ Oph that has frequently been used to study diffuse molecular gas in optical/UV absorption. We also gathered comparable information from the literature to produce a larger sample of observations of the carbon monoxide isotopologues from diffuse molecular gas covering a wider range of values of the profile-integrated ¹²CO emission brightness W_{CO}.

Observations of the individual regions observed here were discussed in Section 3 and illustrated in Figures 1-5. The systematics of the carbon monoxide isotopologues were discussed in Section 4 and summarized in Figure 6. As shown in Figure 6 there is a gradual increase in the W_{13}/W_{CO} isotopologic integrated brightness ratio from $1/40 \leq W_{13}/W_{CO} \leq 1/20$ at $0.8 \text{ K-km s}^{-1} \lesssim W_{CO} \lesssim 4 \text{ K-km s}^{-1}$ to higher values 1:15 - 1:5 with much larger scatter (factor 5) at larger W_{CO} . Carbon monoxide column densities and line brightnesses are largely synonymous, with $W_{CO} \approx N(\text{CO})/(10^{15} \text{ cm}^{-2})$ for $W_{CO} \lesssim 5 \text{ K-km s}^{-1}$ and $N(\text{CO}) \lesssim 5 \times 10^{15} \text{ cm}^{-2}$ at densities $n(\text{H}) \gtrsim 100 \text{ cm}^{-2}$ for all isotopologues. The implication, made clear in the right side panel in Figure 6 showing both ratios for both the column density and intensity ratios, is that the isotopologic intensity ratios observed at $W_{CO} \lesssim 5 \text{ K-km s}^{-1}$ are very close to the ratio of column densities even when comparatively large values $1/40 \lesssim W_{13}/W_{CO} \lesssim 1/15$ are observed. Departures from the intrinsic ratio $^{13}\text{C}/^{12}\text{C} = 1/62$ result from isotopic C^+ exchange that dominates selective photodissociation across the entire observed range in W_{CO} .

The relationship between CO brightness and column density flattens for $W_{CO} \gtrsim 5 \text{ K-km s}^{-1}$ where $N(\text{CO})/W_{CO} > 10^{15} \text{ cm}^{-2} (\text{K-km s}^{-1})^{-1}$, but substantial enhancement of ^{13}CO persists over the entire observed range of W_{CO} , and whenever C^+ is the dominant form of gas-phase carbon (and not otherwise). Ratios $N(^{13}\text{CO})/N(^{12}\text{CO})$ as small as 1/60 are expected only at very very small $N(\text{CO})$ where there is no self-shielding, in regions of very high UV illumination, or when the gas phase carbon has fully recombined from C^+ to CO. The only sure way to avoid factor $f > 1$ enhancement of ^{13}CO is to be certain that the fraction of free gas-phase ^{12}C in ^{12}CO exceeds $1/f$. Of course it is pointless to derive $N(\text{CO})$ if the ultimate goal is to determine $N(\text{H}_2)$ when the relative CO abundance $N(\text{CO})/N(\text{H}_2)$ is as small and variable as it is in diffuse molecular gas.

6.2. C^{18}O

C^{18}O is observed in UV absorption to be depleted by a factor three below the value $N(\text{C}^{18}\text{O}):N(^{12}\text{CO}) = 1:520$ corresponding to the intrinsic isotopic relative abundance ratio $^{18}\text{O}/^{12}\text{C}$. We obtained limits $W_{18}/W_{13} < 1/40 - 1/20$ along a handful of sight-lines with bright ^{13}CO lines, vs an intrinsic ratio $^{18}\text{O}/^{13}\text{C} = 1/8.4$, see Figure 7. Selective photodissociation of C^{18}O is present in our data but the gas is also enhanced in ^{13}CO and the emission observations did not constrain the depletion of C^{18}O at the levels detected in UV absorption despite the very low brightness levels to which we chased the C^{18}O emission. Nonetheless high isotopologic brightness ratios W_{13}/W_{18} are expected to be a hallmark of emission from diffuse molecular gas.

6.3. $\text{CS } J=2-1$ vs. CO and HCO^+

In Figure 8 we showed that CS $J=2-1$ emission abruptly brightens from $0.03 - 0.04 \text{ K-km s}^{-1}$ to 0.2 K-km s^{-1} over a narrow range of CO brightness $W_{CO} = 10-12 \text{ K-km s}^{-1}$ and is bimodal with respect to the brightness of HCO^+ with a separation of a factor 4. As noted in Section 5.2, The $J=2-1$ line of CS and the $J=1-0$ line of HCO^+ are both in the weak excitation limit where W_{CS} and W_{HCO^+} are proportional to $N(\text{CS})$ and $N(\text{HCO}^+)$, respectively, so the bimodality of the brightnesses represents bimodality of the $N(\text{CS})/N(\text{HCO}^+)$ ratio with values 5 and 1.25, as indicated in Figure 9. Bistable chemical solutions for sulfur-bearing molecules are now well-studied for dense gas but are not expected in diffuse molecular gas where the electron fraction is high.

6.4. HCO^+ and CO

Comparisons between W_{CO} and W_{HCO^+} are shown in Figure 8 at left, and, on a logarithmic scale with model results superimposed, in Figure 10. As discussed in Section 5.2, HCO^+ plays a special dual role as progenitor of CO via thermal recombination with ambient electrons and as an H_2 -tracer with fixed relative abundance $N(\text{HCO}^+)/N(\text{H}_2) = 3 \times 10^{-9}$. Given that the HCO^+ emission line brightness $W_{\text{HCO}^+} \propto$

$N(\text{HCO}^+) \propto N(\text{H}_2)$ is mostly due to rotational excitation by electrons with which HCO^+ also recombines to form CO, W_{HCO^+} traces $N(\text{H}_2)$ while the $W_{\text{HCO}^+}/W_{\text{CO}}$ brightness ratio traces both the CO photodestruction rate and the CO abundance relative to H_2 . The chemical model that explains the presence of CO through HCO^+ recombination also accounts for the baseline level of HCO^+ emission 0.03 K-km s^{-1} and $\log(W_{\text{HCO}^+}/W_{\text{CO}}) = -2 \pm 0.3$ at modest density $n(\text{H}) \approx 100 \text{ cm}^{-3}$. The peak HCO^+ brightness and the scatter in the $W_{\text{HCO}^+}/W_{\text{CO}}$ brightness ratio both increase considerably for $W_{\text{CO}} \gtrsim 10 \text{ K-km s}^{-1}$. We modeled this as arising from some combination of stronger illumination (increasing the CO photodissociation rate and the required column densities of H_2 and HCO^+ required to produce a given $N(\text{CO})$ and W_{CO}), and higher density.

The low-light models that strongly fractionate carbon monoxide and enhance ^{13}CO are very efficient at producing H_2 and CO, and reproduce the observed CO column density and brightness $W_{\text{CO}} \lesssim 5 \text{ K-km s}^{-1}$ at reddening well below even 0.1 magnitudes in Figure 10. The CO hotspots with $W_{\text{CO}} = 5 \text{ K-km s}^{-1}$ seen in the vicinity of sightlines toward extragalactic continuum sources probably represent the sort of localized regions with higher density and increased optical shielding that are seen in numerical models of turbulent flow in diffuse molecular gas at the $\text{HI} \rightarrow \text{H}_2$ transition. In Section 5.3 we gave a numerical example showing that the column densities required to produce the observed CO emission imply mildly sub-pc sized regions subtending angular sizes of about $10'$ ($256 \text{ cm}^{-2}/n(\text{H}))^{-2}$ at a distance of 200 pc, as observed. These hotspots are embedded in a more broadly-distributed, weakly CO-emitting, less fully-molecular medium having density a few times lower, which is most easily detected in HCO^+ absorption while making a noticeable contribution to the HCO^+ emission as discussed in Section 5.2.

6.5. *The bright CO emission contribution of diffuse molecular gas*

Although more attention has recently been paid to conditions under which CO is not detectable, CO actually radiates exceptionally brightly on a per-molecule basis in subthermally-excited diffuse molecular gas. The CO column density producing $W_{\text{CO}} \approx 1 - 10 \text{ K-km s}^{-1}$ in diffuse, partially molecular gas, $N(\text{CO}) \approx 10^{15} - 10^{16} \text{ cm}^{-2}$ is far smaller than from the colder, denser fully-molecular gas in dark clouds, where C^+ has fully recombined to CO at kinetic temperatures of 10-12 K. At $A_V = 5 \text{ mag}$ and $N(\text{CO})/N(\text{H}_2) = 8 \times 10^{-5}$, the same brightness would be produced with $N(\text{CO}) \approx 5 \times 10^{17} \text{ cm}^{-2}$ in a fully molecular gas.

For CO, as with other molecules at the threshold of detectability, column density is the main determining factor. Any density capable of fostering a CO chemistry putting 0.1% or more of the free gas phase carbon into CO at 1 magnitude extinction will put enough energy into the $J=1-0$ CO line to render its emission detectable at a level $W_{\text{CO}} \gtrsim 0.1 \text{ K-km s}^{-1}$. Detectability at the 1 K-km s^{-1} level requires $N(\text{CO}) = 10^{15} \text{ cm}^{-2}$ for $n(\text{H}) \gtrsim 100 \text{ cm}^{-3}$, while the expected free gas-phase carbon column density at 1 magnitude of optical extinction is $4 \times 10^{17} \text{ cm}^{-2}$, implying that only 2.5% of the free gas-phase carbon need be in CO. For diffuse molecular gas where $N(\text{CO})$ and W_{CO} are proxies for each other around the $W_{\text{CO}} = 1 \text{ K-km s}^{-1}$ threshold of detectability in wide-field surveys, $N(\text{H}_2)/W_{\text{CO}} \propto N(\text{H}_2)/N(\text{CO})$, and it is the CO abundance that determines the CO- H_2 conversion factor and the ability of CO to serve as an H_2 surrogate.

6.6. *Dense gas tracers also trace diffuse gas*

Species like HCO^+ and, especially, HCN, having higher dipole moments than CO (2-4 Debye vs 0.11 Debye) and higher ‘‘critical densities’’ (Shirley 2015) are taken to trace ‘‘dense’’ gas, ie molecular gas at higher density than that traced by the more easily excited and (independently) more

ubiquitous CO. $W_{\text{HCO}^+}/W_{\text{CO}}$ and $W_{\text{HCN}}/W_{\text{CO}}$ ratios 0.01 - 0.02 are observed in the disk of the Milky Way (Liszt 1995; Helfer & Blitz 1997) and other galaxies (Bigiel et al. 2015; Jiménez-Donaire et al. 2019). CS emission is comparably bright in the Milky Way.

Ratios $W_{\text{HCO}^+}/W_{\text{CO}} = 1\text{-}2\%$ are also characteristic of our sightlines having weak CO emission $W_{\text{CO}} = 1\text{-}2 \text{ K-km s}^{-1}$ and are explained by models of modest density $n(\text{H}_2) < 100 \text{ cm}^{-3}$ (Figure 10). The $W_{\text{HCO}^+}/W_{\text{CO}}$ brightness ratio in diffuse gas is an artifact of the CO formation chemistry and $W_{\text{HCO}^+}/W_{\text{CO}}$ is higher for weaker W_{CO} in diffuse molecular gas because HCO^+ persists under conditions where CO is poorly shielded. Why similar ratios should be observed across a wide range of supposedly different environments in the Milky Way and other galaxies is an open question.

HCN J=1-0 emission is perhaps the gold standard “dense gas” tracer but observations of HCN in diffuse molecular gas are scarce. Unlike HCO^+ or CS, the HCN brightness is divided among three hyperfine components that are blended in extragalactic but seen separately in emission that is resolved spatially, as is the case here. Toward BL Lac Peak 1 $W_{\text{HCN}}/W_{\text{HCO}^+} = 1.05 \pm 0.12$ and $W_{\text{HCN}}/W_{\text{CO}} = 0.017 \pm 0.001$ (Table 2 and Appendix B). The main HCN hyperfine component was detected 30' south of ζ Oph (Liszt 1997) where $W_{\text{HCO}^+}/W_{\text{CO}} = 0.019 \pm 0.001$ and $W_{\text{HCN}}/W_{\text{CO}} \approx 0.011 \pm 0.002$ if the three hyperfine components of HCN emit in the LTE ratio 5:9:1.

Thus, 1-2% $W_{\text{HCO}^+}/W_{\text{CO}}$ and $W_{\text{HCN}}/W_{\text{CO}}$ brightness ratios may arise in gas having very modest density, $n(\text{H}_2) \gtrsim 100 \text{ cm}^{-3}$ for the better-sampled HCO^+ data in Figure 10. By contrast CS J=2-1 emission was detected in our data only when $W_{\text{CO}} \approx 10 \text{ K-km s}^{-1}$, which is likely to be denser according to Figure 10. CS J=2-1 emission is less commonly observed now (eg Bigiel et al. (2015); Jiménez-Donaire et al. (2019)) because it is not covered by the tunings that simultaneously observe CO and the high dipole moment species C_2H , HCN

and HCO^+ with recent broadband $\lambda 3\text{mm}$ IRAM receivers.

6.7. Separating dense and diffuse gas

Our observations described the qualities of emission from the diffuse molecular gas, not the quantity of this gas in the ISM at large. Roman-Duval et al. (2016) separated the dense and diffuse gas contributions observed in ^{12}CO , ^{13}CO and CS across the Milky Way disk, concluding that the diffuse gas fraction increased from 10% at the peak of the molecular ring at $R \approx R_0/2$ to 50% at $R = R_0$, the Solar Circle. A comparable diffuse gas fraction at the Solar Circle, 40%, was derived by comparing the ^{12}CO emissivity measured in galactic plane surveys with the brightness of emission from diffuse molecular gas observed locally at high galactic latitudes, as done here, extrapolated to a face-on view through the disk Liszt et al. (2010). Some 40% of the emission viewed from outside would arise from diffuse molecular gas well outside regions of higher density or extinction.

The ratio of ^{12}CO and ^{13}CO emissivities A_{CO}/A_{13} measured in galactic plane surveys¹, the quantity measured in galactic plane surveys with units of $\text{K-km s}^{-1} \text{ kpc}^{-1}$ (Burton & Gordon 1978) can be related to the mean matter density: $A_{\text{CO}} = dW_{\text{CO}}(R)/dR \propto \langle n(\text{H}_2) \rangle / \lambda \propto \langle n(\text{H}_2) \rangle$ if $N(\text{H}_2) \propto W_{\text{CO}}$ via the CO- H_2 conversion factor and λ is the line of sight geometric mean free path between emitting gas parcels (Liszt & Gerin 2016) changes by a factor two or more across the disk of the Milky Way inside the Solar Circle (Roman-Duval et al. 2016; Liszt et al. 1984), from $A_{\text{CO}}/A_{13} \approx 5$ to $A_{\text{CO}}/A_{13} \gtrsim 10$, even as the $W_{\text{HCO}^+}/W_{\text{CO}}$ brightness ratio does not show a comparable change (Liszt 1995; Helfer & Blitz 1997). Likewise, the two EMPIRE galaxies having factor ≈ 2 gradients in W_{CO}/W_{13} across their disks (NGC 4254 and the oddball NGC 628) do not have pronounced gradients in $W_{\text{HCO}^+}/W_{\text{CO}}$ (Jiménez-Donaire et al.

¹ A_{CO}

2019). This is consistent with the inference that $W_{\text{HCO}^+}/W_{\text{CO}} \approx 1 - 2\%$ across environments in galaxy disks.

The $^{12}\text{CO}/^{13}\text{CO}$ brightness ratio ranges from 10 to 18 with a mean $\langle^{12}\text{CO}/^{13}\text{CO}\rangle \approx 13 \pm 3$ around $R = 5$ kpc in the 9 EMPIRE galaxies Jiménez-Donaire et al. (2019). Such high ratios are not seen in the Milky Way except well outside the Solar Circle where the diffuse gas fraction is large and the CO-H₂ conversion factor is expected to be higher owing to lower metallicity (Bolatto et al. 2013). The $^{12}\text{CO}/^{13}\text{CO}$ brightness ratio does not vary much across the disks of 6-7 of the 9 EMPIRE galaxies, even as 2 of 3 of those galaxies lacking gradients in W_{CO}/W_{13} show the $^{13}\text{CO}/\text{C}^{18}\text{O}$ brightness ratio increasing outward from $\approx 6 - 8$ to $\gtrsim 20$ (Jiménez-Donaire et al. 2017). There is no comparable information on the variation of the $^{13}\text{CO}/\text{C}^{18}\text{O}$ brightness ratio across the Milky Way disk. The constant Milky Way value 8.3 for the $^{13}\text{CO}/\text{C}^{18}\text{O}$ brightness ratio quoted by Jiménez-Donaire et al. (2017) was determined (Wouterloot et al. 2008) by observing CO isotopolog emission toward the CO-brightest and densest parts of star-forming regions like W49 and W3 and was only intended to find the intrinsic isotopic abundance ratio $[\text{O}^{13}]/[\text{O}^{18}]$, not the brightness ratio in the Milky Way disk ISM.

High $^{12}\text{CO}/^{13}\text{CO}$ brightness ratios and $^{13}\text{CO}/\text{C}^{18}\text{O}$ brightness ratio gradients suggest a prominent role for diffuse molecular gas in external galaxy disks and, as noted in Section 6.7,

such gas emits with $W_{\text{HCN}}/W_{\text{CO}}$ and $W_{\text{HCO}^+}/W_{\text{CO}}$ brightness ratios of 1-2% that are characteristic of external galaxy disks. Dense gas fractions determined from the emission of so-called dense gas tracers should be corrected for this effect.

ACKNOWLEDGMENTS

I thank the staff of the ARO, Dr. Lucy Ziurys (former ARO Director) and especially the telescope operators at the ARO Kitt Peak 12m telescope for their support. Comments by the anonymous referee helped to clarify my intentions for this work.

The Kitt Peak 12-Meter Radio Telescope is operated by the Arizona Radio Observatory (ARO), which is part of Steward Observatory at the University of Arizona. The State of Arizona provides major financial support for ARO operations; additional funding comes from the National Science Foundation Major Research Instrumentation (MRI) grant to the University of Arizona for Development of a State-of-the-Art Multiband Receiver for Arizona Radio Observatory's New ALMA Antenna (PI Ziurys AST-1531366).

The National Radio Astronomy Observatory is a facility of the National Science Foundation operated under cooperative agreement by Associated Universities, Inc. This manuscript was largely finished while the author was enjoying the hospitality of the ITU-R and the eponymous Sheraton Hotels in Sharm El-Sheikh and Waikiki.

Facility: ARO Kitt Peak 12m

Software: DRAWSPEC

APPENDIX

A. DATA

Profile integrals for the new emission data presented here are given in Table A.1

B. AN EXTENDED INVENTORY OF EMISSION NEAR BL Lac

Figure B.1 shows emission profiles toward Peak 1 near BL Lac including HCN, HNC and C₂H that are not discussed in the main text. HCN and HNC column densities measured in absorption in diffuse gas are discussed Liszt & Lucas (2001) and observations of C₂H and other small hydrocarbons are discussed in

Table 2. Profile integrals for new data presented here

Source	RA	Decl	l	b	Velocity	¹² CO	¹³ CO	C ¹⁸ O
Source	hh.mmss	dd.mmss	d.dddd	d.dddd	km s ⁻¹	K km s ⁻¹	K km s ⁻¹	K km s ⁻¹
B0736	7.39180	1.37046	216.9897	11.3806	4.5..7.5	0.78(0.03)	0.048(0.02)	
B0736Pk	7.39380	1.35246	217.0528	11.4423		4.15(0.41)	0.186(0.017)	
B0954	9.58472	65.33547	147.7463	43.1316	2.5..5.0	1.63(0.10)	0.025(0.010)	
B0954WPk	9.59355	65.33547	145.6831	43.2011		6.88(0.22)	0.900(0.015)	(0.011)
B1954	19.55427	51.31485	85.2984	11.7569	0..2	1.59(0.05)	0.055(0.015)	
B1954WPk	19.54212	51.35485	85.2535	11.9737	-1..1	3.12(0.03)	1.000(0.011)	(0.008)
B1954EPk	19.55298	51.32085	85.28686	11.7886	0..1.5	2.95(0.03)	0.240 (0.011)	
B2251	22.53572	16.08534	86.11088	-38.1838	-11..-8	0.78(0.02)	0.022(0.007)	
B2251Pk	22.53424	16.12134	86.0856	-38.1037		5.20(0.03)	0.470(0.015)	(0.010)
B0528	5.30564	13.31155	191.4148	-11.0534	0..3	(0.04)	(0.008)	
B0528A	5.30537	13.28151	191.2594	-11.2337		10.05(0.25)	0.537 (0.009)	
B0528T	5.31156	13.20151	191.5765	-11.0467		7.77(0.18)	0.187(0.022)	
B0528pT	5.30495	13.30151	191.3768	-11.0507		0.90(0.21)	<0.040	
B0528	5.30564	13.31155	191.4148	-11.0534	8..12	2.20(0.04)	0.107(0.008)	
B0528A	5.30537	13.28151	191.2594	-11.2337		2.22(0.23)	0.075(0.008)	
B0528T	5.31156	13.20151	191.5765	-11.0467		6.30(0.16)	0.808(0.019)	
B0528D	5.29561	13.30151	191.5765	-11.0467		10.58(0.20)	2.104(0.015)	
B0528N	5.30591	13.44351	191.1905	-10.8917		8.40(0.31)	1.602(0.101)	
B0528pW	5.30482	13.32351	191.3402	-11.0344		6.21(0.20)	0.804(0.111)	
B0528pT	5.30495	13.30151	191.3768	-11.0507		5.97(0.19)	0.920(.120)	
BLac	22.02433	42.16399	92.5895	-10.4411	-3.5..0.5	5.14(0.11)	0.766(0.022)	(0.010)
BLac Peak1	22.03010	42.2018	92.6711	-10.42462		12.38(0.42)		
BLac Peak2	22.03177	42.16321	92.6740	-10.5073		9.62(0.44)		
BLac Peak3	22.03116	42.16340	92.6591	-10.4955		10.31(0.42)		
BLac Peak4	22.02514	42.16019	92.6032	-10.4647		11.44(0.35)		
L121-Z0	16.34571	-12.49496	3.9533	22.6756	-2.5..-0.7	11.42(0.104)	1.400(0.036)	(0.011)
L121-Z1	16.34034	-12.37174	3.9917	22.9756		5.54(0.13)	0.137(0.027)	
L121-Z2	16.35372	-12.52564	4.0144	22.5144		9.61(0.15)	0.822(0.029)	
L121-Z3	16.34467	-12.42082	4.0366	22.7866		8.97(0.11)	0.819(0.024)	
L121-Z4	16.35279	-12.39184	4.1866	22.6811		5.74(0.11)	0.210(0.020)	
L121-Z5	16.35172	-12.22472	4.3972	22.8811		2.14(0.13)	(0.025)	
L121-Z6	16.35283	-12.11216	4.5922	22.9589		1.00(0.15)	(0.020)	
L121-Z7	16.36532	-12.21271	4.67 00	22.5811		11.54(0.16)	0.660(0.020)	
L121-Z8	16.34506	-11.43081	4.9028	23.3630		4.48(0.20)	0.300(0.011)	(0.011)
L121-Z9	16.34491	-11.35599	5.0028	23.4389		3.67(0.11)	0.168(0.021)	
L121-Z4	16.35279	-12.39184	4.1866	22.6811	-0.7..1.7	9.34(0.11)	1.161(0.032)	
L121-Z5	16.35172	-12.22472	4.3972	22.8811		5.97(0.13)	0.312(0.031)	
L121-Z6	16.35283	-12.11216	4.5922	22.9589		7.75(0.16)	0.587(0.022)	
L121-Z8	16.34506	-11.43081	4.9028	23.3630		12.02(0.14)	1.381(0.042)	(0.012)
L121-Z9	16.34491	-11.35599	5.0028	23.4389		13.91(0.12)	1.364(0.028)	

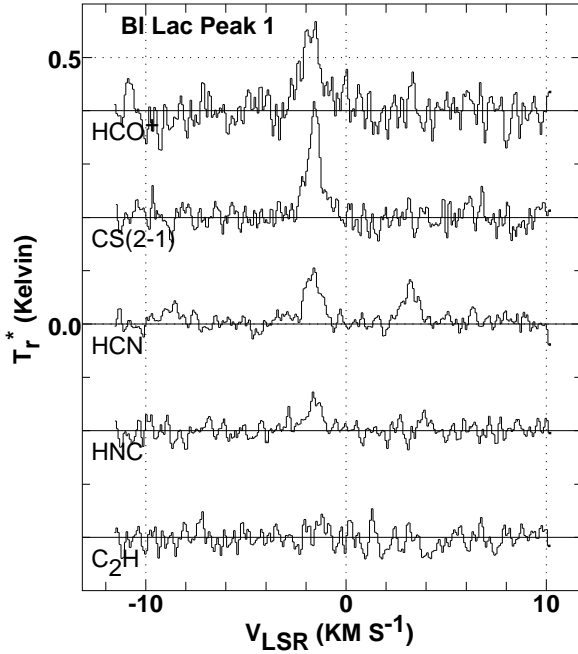


Figure 11. A fuller inventory of molecular emission toward Peak 1 near BL Lac.

Lucas & Liszt (2000) and Liszt et al. (2012). The profile integrals are 0.218 ± 0.007 K-km s⁻¹ for HCN (all three components), 0.067 ± 0.009 K-km s⁻¹ for HNC, and 0.017 ± 0.009 K-km s⁻¹ for C₂H.

C. N(CS) AND HCO⁺ OBSERVED IN ABSORPTION

Figure C.1 shows CS and HCO⁺ column densities derived in absorption, with data as in Figure 4 of Lucas & Liszt (2002) but using an updated permanent dipole moment $\mu_D = 3.92$ Debye (Mount et al. 2012) to calculate N(HCO⁺), instead of 4.07 Debye. The ensemble-averaged CS/HCO⁺ abundance ratio is $\langle N(\text{CS}) \rangle / \langle N(\text{HCO}^+) \rangle = 1.27$ and the mean CS/HCO⁺ ratio is $\langle N(\text{CS}) / N(\text{HCO}^+) \rangle = 1.66 \pm 1.32$. Although there is one datapoint with $W_{\text{CS}} / W_{\text{HCO}^+} \approx 5$ in Figure C.2, the bimodality seen in CS and HCO⁺ emission in Figure 8 is not present in the absorption sample, consistent with the weak CO emission that characterizes the sightlines toward the continuum sources.

REFERENCES

- Berné, O., Marcelino, N., & Cernicharo, J. 2010, *Nature*, 466, 947
- Bialy, S., Neufeld, D., Wolfire, M., Sternberg, A., & Burkhardt, B. 2019, *ApJ*, 885, 109
- Bigiel, F., Leroy, A. K., Blitz, L., et al. 2015, *ApJ*, 815, 103
- Boger, G. I., & Sternberg, A. 2006, *ApJ*, 645, 314
- Bolato, A. D., Wolfire, M., & Leroy, A. K. 2013, *ARA&A*, 51, 207
- Burton, W. B., & Gordon, M. A. 1978, *A&A*, 63, 7
- Charnley, S. B., & Markwick, A. J. 2003, *A&A*, 399, 583
- Dame, T. M., Hartmann, D., & Thaddeus, P. 2001, *ApJ*, 547, 792
- Draine, B. T. 2011, *Physics of the Interstellar and Intergalactic Medium* (Princeton University Press, 2011. ISBN: 978-0-691-12214-4)
- Dufour, G., & Charnley, S. B. 2019, *ApJ*, 887, 67
- Gerin, M., Falgarone, E., Joulain, K., et al. 1997, *A&A*, 318, 579
- Godard, B., Falgarone, E., & Pineau des Forêts, G. 2014, *A&A*, 570, A27
- Goldreich, P., & Kwan, J. 1974, *ApJ*, 189, 441

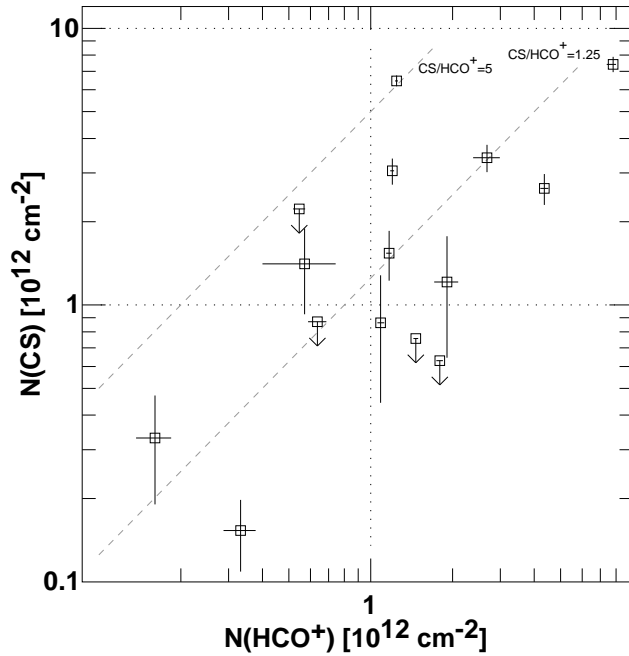


Figure 12. CS and HCO⁺ column densities measured in absorption, see Appendix C

- Goldsmith, P. F., Heyer, M., Narayanan, G., et al. 2008, *ApJ*, 680, 428
- Grenier, I. A., Casandjian, J.-M., & Terrier, R. 2005, *Science*, 307, 1292
- Helfer, T. T., & Blitz, L. 1997, *ApJ*, 478, 233
- Hensley, B. S., & Draine, B. T. 2017, *ApJ*, 836, 179
- Heyer, M., Goldsmith, P. F., Yıldız, U. A., et al. 2016, *MNRAS*, 461, 3918
- Jiménez-Donaire, M. J., Cormier, D., Bigiel, F., et al. 2017, *ApJ*, 836, L29
- Jiménez-Donaire, M. J., Bigiel, F., Leroy, A. K., et al. 2019, *ApJ*, 880, 127
- Le Bourlot, J., Pineau des Forets, G., Roueff, E., & Schilke, P. 1993, *ApJ*, 416, L87
- Le Petit, F., Roueff, E., & Le Bourlot, J. 2002, *A&A*, 390, 369
- Lee, H.-H., Roueff, E., Pineau des Forets, G., et al. 1998, *A&A*, 334, 1047
- Liszt, H. 2014a, *ApJ*, 783, 17
- 2014b, *ApJ*, 780, 10
- Liszt, H., Gerin, M., & Grenier, I. 2018, *A&A*, 617, A54
- 2019, *A&A*, 627, A95
- Liszt, H., & Lucas, R. 2001, *A&A*, 370, 576
- Liszt, H., Sonnentrucker, P., Cordiner, M., & Gerin, M. 2012, *ApJ*, 753, L28
- Liszt, H. S. 1995, *ApJ*, 442, 163
- 1997, *A&A*, 322, 962
- 2007, *A&A*, 476, 291
- 2008, *A&A*, 492, 743
- 2011, *A&A*, 527, A45
- 2012, *A&A*, 538, A27
- 2015, *ApJ*, 799, 66
- 2017, *ApJ*, 835, 138
- Liszt, H. S., Burton, W. B., & Xiang, D.-L. 1984, *A&A*, 140, 303
- Liszt, H. S., & Gerin, M. 2016, *A&A*, 585, A80
- Liszt, H. S., & Lucas, R. 1998, *A&A*, 339, 561
- Liszt, H. S., & Pety, J. 2012, *A&A*, 541, A58
- 2016, *ApJ*, 823, 124
- Liszt, H. S., Pety, J., & Lucas, R. 2010, *A&A*, 518, A45+
- Liszt, H. S., Pety, J., & Tachihara, K. 2009, *A&A*, 499, 503
- Lucas, R., & Liszt, H. S. 1996, *A&A*, 307, 237
- 2000, *A&A*, 358, 1069
- 2002, *A&A*, 384, 1054
- Magnani, L., Blitz, L., & Mundy, L. 1985, *ApJ*, 295, 402
- Mount, B. J., Redshaw, M., & Myers, E. G. 2012, *PhRvA*, 85, 012519
- Planck Collaboration, Fermi Collaboration, Ade, P. A. R., et al. 2015, *A&A*, 582, A31
- Roman-Duval, J., Heyer, M., Brunt, C. M., et al. 2016, *ApJ*, 818, 144
- Roueff, E., Loison, J. C., & Hickson, K. M. 2015, *A&A*, 576, A99

- Schlegel, D. J., Finkbeiner, D. P., & Davis, M. 1998, *ApJ*, 500, 525
- Shetty, R., Glover, S. C., Dullemond, C. P., & Klessen, R. S. 2011, *MNRAS*, 412, 1686
- Shirley, Y. L. 2015, *Publ. Astron. Soc. Pac.*, 127, 299
- Sofia, U. J., Lauroesch, J. T., Meyer, D. M., & Cartledge, S. I. B. 2004, *ApJ*, 605, 272
- Szucs, L., Glover, S. C. O., & Klessen, R. S. 2016, *MNRAS*, 460, 82
- Tritsis, A., Federrath, C., Schneider, N., & Tassis, K. 2018, *MNRAS*, 481, 5275
- Valdivia, V., Godard, B., Hennebelle, P., et al. 2017, *A&A*, 600, A114
- Wakelam, V., Herbst, E., Selsis, F., & Massacrier, G. 2006, *A&A*, 459, 813
- Wolfire, M. G., Hollenbach, D., & McKee, C. F. 2010, *ApJ*, 716, 1191
- Wolfire, M. G., Hollenbach, D., McKee, C. F., Tielens, A. G. G. M., & Bakes, E. L. O. 1995, *ApJ*, 443, 152
- Wolfire, M. G., McKee, C. F., Hollenbach, D., & Tielens, A. G. G. M. 2003, *ApJ*, 587, 278
- Wouterloot, J. G. A., Henkel, C., Brand, J., & Davis, G. R. 2008, *A&A*, 487, 237
- Zucker, C., Speagle, J. S., Schlafly, E. F., et al. 2019, *ApJ*, 879, 125